University of Texas Rio Grande Valley

ScholarWorks @ UTRGV

Theses and Dissertations

5-2021

# Characterization of the RF Magnetron Sputtered p-Si & n-Si on Si Substrate and Effect of Process Parameters on their Structural & Electrical Properties

Prosanto Biswas
*The University of Texas Rio Grande Valley*

Follow this and additional works at: https://scholarworks.utrgv.edu/etd

Part of the Electrical and Computer Engineering Commons

## Recommended Citation

Biswas, Prosanto, "Characterization of the RF Magnetron Sputtered p-Si & n-Si on Si Substrate and Effect of Process Parameters on their Structural & Electrical Properties" (2021). *Theses and Dissertations*. 621.
https://scholarworks.utrgv.edu/etd/621

This Thesis is brought to you for free and open access by ScholarWorks @ UTRGV. It has been accepted for inclusion in Theses and Dissertations by an authorized administrator of ScholarWorks @ UTRGV. For more information, please contact justin.white@utrgv.edu, william.flores01@utrgv.edu.

# CHARECTERIZATION OF THE RF MAGNETRON SPUTTERED p-Si & n-Si ON Si SUBSTRATE AND EFFECT OF PROCESS PARAMETERS ON THEIR STRUCTURAL & MORPHOLOGICAL PROPERTIES

A Thesis

by

PROSANTO BISWAS

Submitted to the Graduate College of
The University of Texas Rio Grande Valley
In partial fulfillment of the requirements for the degree of

MASTER OF SCIENCE IN ENGINEERING

May 2021

Major Subject: Electrical Engineering

# CHARECTERIZATION OF THE RF MAGNETRON SPUTTERED p-Si & n-Si ON Si SUBSTRATE AND EFFECT OF PROCESS PARAMETERS ON THEIR STRUCTURAL & MORPHOLOGICAL PROPERTIES

A Thesis
by
PROSANTO BISWAS

COMMITTEE MEMBERS

Dr. Hasina F. Huq
Chair of Committee

Dr. Heinrich Foltz
Committee Member

Dr. Ahmed Touhami
Committee Member

May 2021

Copyright 2021 Prosanto Biswas
All Rights Reserved

ABSTRACT

Biswas, Prosanto., Characterization of the RF Magnetron Sputtered p-Si, n-Si & $SiO_2$ on Si Substrate and Effect of Process Parameters on Their Structural & Morphological Properties. Master of Science (MS), May 2021, 66 pp., 13 tables, 35 figures, 63 references, 22 titles.

In our work, we applied Taguchi Signal-to-noise (SNR) analysis to investigate the effect of varying three process parameters, namely- sputtering power, working pressure, and Ar gas flow rate on the surface and morphological properties of the RF sputtered p-Si and n-Si on Si substrate. We also inspected the contribution of process parameters on those properties by applying Analysis of Variance (ANOVA). Characteristics of thin films fabricated by RF magnetron sputtering vary with the recipes. Process parameters such as power, pressure, process gas flow rate, substrate temperature, and target to substrate distance determine the quality of the thin films. Some of these parameters contribute more significantly towards a specific property of the thin film than other parameters. For RF sputtered p-Si on Si Substrate, we tried to determine which parameters contribute most to surface properties like grain size, micro-stress, and surface roughness and the effect of variation of these parameters. We applied the same procedure for n-Si thin films. Using 2" diameter targets of thickness 0.125" each, thin films of two kinds were fabricated on Si substrate using RF magnetron sputtering system. For each material (p-Si / n-Si), two sets of inputs for the three mentioned process parameters were chosen; for power, we chose 100W, 150W, and 200W; 5mTorr, 10mTorr, and 15mTorr were chosen for pressure, and we varied Ar gas flow rate at 5, 10 and 15 sccm (standard cubic centimeter per minute). We applied

the Taguchi Design of experiments method to find out the optimized process parameter combination. By performing Taguchi L9 orthogonal array, nine combinations of the recipe were prepared for sputtering p-Si and n-Si. The surface and morphological properties of those nine samples were therefore inspected. We studied surface roughness (form AFM & Profilometer), grain size and shape ( from XRD diffractometer) and micro-stress (from W-H plot). Signal-to-noise (SNR) analysis presents how the properties like roughness and grain size change with the process parameters' variation. We found that among the three process parameters, the contribution of sputtering power towards surface roughness and Ar pressure towards grain size are the greatest. We also observed that more sputtering power resulted in smoother surfaces and larger grain sizes. No significant effect was found for Ar gas flow rate from ANOVA test.

# DEDICATION

The completion of my master's studies would not have been possible without the love and support of my family and friends. I dedicate this work to my mother Anita Biswas and my father Niher Ranjon Biswas, wholeheartedly inspired, motivated, and supported me to accomplish this degree. Thank you for your love and patience.

## ACKNOWLEDGMENTS

First, I would like to acknowledge my supervisor, Dr. Hasina F. Huq, for her support and guidance. Her continuous mentorship, along with her excellent vision and expertise in the field of Electrical Engineering, really motivated my journey so far. I am proud to be a member of the Sputtering System Laboratory under her supervision. Besides, I would also like to mention my fellow colleagues from whom I got wonderful support and technical assistance. Particularly, I would mention Sajid Mahfuz Uchayash- who has a tremendous vision and dedication towards his work. Also, I am very thankful to Andres Ochoa, especially for his training to operate the sputtering system, Muhtasim Ul Karim for his technical help to operate the XRD machine and Al Mazedur Rahman for his contribution in the statistical analysis. I am grateful to the Department of Electrical Engineering-UTRGV and the Graduate College-UTRGV. Then, I would like to humbly express my gratitude towards my department's faculties—especially my thesis committee members, Dr. Heinrich Foltz, and Dr. Ahmed Touhami from the Department of physics for guiding me through my thesis. I am also very thankful to Dr. Parwinder Grewal for his strong support to all the graduate students at UTRGV. Without his visionary steps, it would have been impossible to work as a PGRA. Finally, and most importantly, I thank my father, Niher Ranjon Biswas, my mother, Anita Biswas, my sister Nupur Biswas, and my brother-in-law Dr. Sanjib Mondal. I could not do anything without them. Thanks to the Almighty again.

TABLE OF CONTENTS

Page

ABSTRACT ........ iii

DEDICATION ........ v

ACKNOWLEDGEMENTS ........ vi

TABLE OF CONTENTS ........ vii

LIST OF TABLES ........ ix

LIST OF FIGURES ........ x

CHAPTER I. INTRODUCTION ........ 1

1.1 Epitaxial growth of n-Si & p-Si ........ 2

1.2 Magnetron Sputtering ........ 5

1.3 Principle of Plasma Discharge ........ 7

1.4 Ion Bombardment to the Surface ........ 10

1.5 Thesis Outline ........ 12

CHAPTER II. METHODOLOGY ........ 14

2.1 Fabrication ........ 14

2.2 Morphological and Physical Characterization ……………………………………….... 18

2.3 Statistical Analysis …..…………………………………………………..............22

CHAPTER III. MESUREMENTS & CHARACTERIZATION…………………………..….. 28

3.1 X-Ray Diffraction (XRD) …………………………………….…………..... 28

3.2 Williamson-Hall Plot ……………………...…………………………………… 36

CHAPTER IV. RESULTS AND DISSCUSSION ……………………………………….… 43

4.1 Surface Roughness of n-Si ...………………………………………….............. 43

4.2 Crystal formation of n-Si ………………………………………….............. 45

4.3 Micro-strain of n-Si ...………………………………………................... 47

4.4 Surface Roughness of p-Si …………………………………………................ 50

4.5 Crystal formation of p-Si………………………………………….............. 52

CHAPTER V. CONCLUSION and FUTURE WORK………………………………………… 54

REFERENCES ……………………………………………………………………………. 55

APPENDIX……………………………………………………………………………………62

BIOGRAPHICAL SKETCH ……………………………………………………………… 66

LIST OF TABLES

Page

Table 1: Pre-deposition Steps for p-Si and n-Si at 25°C Temperature .................................. 17

Table 2: Pre-deposition Steps for $SiO_2$ at 25°C temperature ........................................... 17

Table 3: Selective sputtering parameters and their levels ................................................ 22

Table 4: Analysis of variance for surface roughness ...................................................... 44

Table 5: Model summary of the regression equation ....................................................... 45

Table 6: Table 6: Summery of n-Si/Si thin films characterizations...................................... 45

Table 7 Analysis of variance for grain size ................................................................. 46

Table 8: Analysis of variance for micro-strain .............................................................. 48

Table 9: Overall measured outputs for p-Si samples ....................................................... 50

Table 10: ANOVA analysis for surface roughness of p-Si ................................................ 51

Table 11: ANOVA analysis for p-Si grain size................................................................. 52

LIST OF FIGURES


Page

Figure 1: Classification of thin film deposition techniques………………………………………… 4

Figure 2: RF magnetron sputtering system main chamber……………………………………..... 6

Figure 3: Scheme of a simple DC electrical discharge ……………………………………….…. 8

Figure 4: Paschen curves for noble gases [1]…………………………………………………… 9

Figure 5: I-V characteristics of DC discharge…………………………………………………... 10

Figure 6: Ion bombardment effect on the surface ……………………….……………………12

Figure 7: Thin films fabrication steps……………………………………….……………….…... 14

Figure 8: Silicon wafer and plane………………………………………...………………... 15

Figure 9: Cleaning steps (a)Di water (b) filtered air (c) ethanol (d) acetone (e) micromixer……16

Figure 10: RF sputtering system (Sputtering system lab, UTRGV) ……………………………18

Figure 11: Plasma creation (a) Ar gas (b) N2 gas ……………………………………………... 18

Figure 12: Surface morphology and crystallography steps……………………………………... 19

Figure 15: Application of Bragg's law in XRD ………………………………………………... 20

Figure 14: Rigaku miniflex benchtop powder x-ray diffractometer …………………………... 20

Figure 15: Marsurf 300c profilometer …………………………………………………………… 21

Figure 16: AFM block diagram ……………………………………………………………….…. 21

Figure 17: Taguchi analysis steps……………………………………………………………..… 24

Figure 18:Standard error (S) of regression …………………………………………………..… 25

Figure 19: Calculation of P-Value ………………………………………………………………26

Figure 20: F- Value comparison …………………………………………………………..…..27

Figure 21: Basic structure of XRD machine ………………………………….…………………... 28

Figure 22: Diffraction from a periodic arrangement of atoms satisfies the Bragg equation …… 29

Figure 23: XRD pattern of RF sputtered n-Si (9 samples) ….…………………………….. 30 - 34

Figure 24: X-ray intensity pattern of 9 p-Si samples ……………………………………... 34

Figure 25: Extracted information content from diffraction peak ………………………………. 38

Figure 26: UDM plot of RF sputtered n-Si (9 samples)……………………………........ 38 - 42

Figure 27: S/N response graph for the surface roughness of the nSi/Si films. ………………… 44

Figure 28: S/N response graph for the grain size of the n-Si thin films. ………………………. 46

Figure 29: S/N response graph for the micro strain of the n-Si thin films …………………… 48

Figure 30: XRD pattern of RF sputtered n-Si in normalized intensity ..................…………... 49

Figure 31: Grain size of all n-Si samples………………………………………………………...49

Figure 32: Micro strain of all n-Si samples ……………………………………………………. 50

Figure 33: S/N response graph for the Grain size of the p-Si films with RF power (Watt), Pressure (mTorr) and Ar Flow (sccm)……………………………………………………51

Figure 34: S/N response graph for the roughness of the p-Si films with RF power (Watt), Pressure (mTorr) and Ar Flow (sccm)…………………………………….……………...53

# CHAPTER 1

# INTRODUCTION

One of the most important materials for semiconductor industries are n-Si, p-Si and SiO2 [1]. Applications of these materials can be categorized according to their fields. Over the past few decades, intensive efforts have been made to grow these materials on top of different kinds of substrates. The demand for these material-based devices are huge and the markets are increasing day after day especially in MEMS industries [2, 3]. As a result, different growing techniques are employed to get better performances . The rapid progress of nanotechnology and MEMS industries has received widespread attention by encompassing a continuous study and developing materials with improved properties revealing breakthroughs [3]. In semiconductor production, doping is the intentional introduction of impurities into an intrinsic semiconductor for the purpose of modulating its electrical, optical, and structural properties [4]. The introduction of impurity atoms into the synthetic process to alter the properties of semiconductor nanocrystals have been designed and prepared from various synthetic routes that usually exhibited some unique features [5]. In the nanocrystalline silicon (nc-Si), the impurity doping particles facilitates the creation of new interfaces and enables the evolution of the advanced material properties. This is due to the dopant such as phosphorus (P) donors and/or boron (B) acceptors being the key technique for controlling the conductivity of the semiconductors. Various dopant and processes have been utilized for the realization of next generation Si-based solar cells and optoelectronic devices. As there are a lot of application of doped silicon ranging

from P-N heterojunctions, Structural layer, or material for devices such as MOSFETs, FINFETs, controlled conductive coatings, N-Silicon based thin film Solar Cells, P-Silicon based Solar cells, Diffusion layer for semiconductor devices, Bio MEMS/NEMS devices, the fabrication process has always been an attention for the researchers for cost effective and better performances approach [6, 7] . The study of thin films of these materials on top of substrates can give a holistic idea about its performances. Among vast processes to grow thin films, RF sputtering has been one of the most effective in terms of performance analysis for n-Si or p-Si [5, 6, 8, 9]. However, information on the states of an impurity dopant for zero-dimensional structures was not elucidated clearly although that observation was critical from the viewpoint of applications to solar cells and opto-electronic devices [4].

### 1.1 Epitaxial growth of n-Si & p-Si

In recent times, phosphorus doped silicon source and drain using the in-situ phosphorus-doped (ISPD) epitaxy process have received interest from researchers because this process permits more accurate positioning of dopant atoms compared with the conventional ion-implantation method [5, 6, 9, 10]. In addition, phosphorus concentration of epitaxially grown ISPD silicon is significantly higher than that of the ion-implanted layer [6] and it is beyond the solid solubility limit of phosphorus in silicon [6, 11]. The conductivity of the epitaxially grown layers is also modified by the grain formation characteristics during ISPD epitaxy process. Exploring strain of the source and drain in other studies by Yeo et al., Bedell et al. and Chu et al. was conducted to improve transistor performance due to the growing need for higher operational efficiency and speed since the 65 nm process technology [12-14]. However only few studies were performed on strain and grain formation during phosphorous doped silicon epitaxy process by RF magnetron sputtering system. Compression or relaxation and large grain formation on nc-

Si with the presence of phosphorus dopant are dependent on various process parameters such as power, pressure, and process gas flow rate. For optimizing the sputtering process parameters this study conducted an experimental design based on the Taguchi method to analyze the effects of power, pressure, and process gas on surface roughness, grain size and strain. Through these studies, it was possible to establish optimal conditions for selective phosphorus doped Si thin film property.

Similar thing is applicable for $SiO_2$. Application of thin/thick films of $SiO_2$ are many. The optical and electrical quality of the crystalline-Si (c-Si) solar cell wafer was optimized by applying $SiO_2$ and effectively used in the world-record efficiency c-Si solar cell produced by the University of New South Wales [15]. Silicon oxide has adjustable forbidden bandwidth that can be served as a light absorption layer of the thin film of amorphous-Si (a-Si) solar cells to improve light absorption efficiency [15]. Thermally grown $SiO_2$ has an ideal refractive index to maximize internal reflection at the solar cell's back [16]. In microelectronic $SiO_2$ is used as dielectric gate layer of MOS and CMOS devices or the thin film transistor due to its superior electrical insulation. In optical industry, it has light-admitting quality, electro-optic modulation function, and optical amplification use [15, 17] with low loss over a wide frequency range, thermal and mechanical stability, and ease of processing [17]. Li et al. [17] of the Australian national university reported Silica thin films for a very large Second-Order Nonlinearity (SON) to make efficient integrated electro-optic devices or modulators in optical telecommunication. In Packaging industry, SiO2 is used as a barrier layer of polymer packaging materials that offer sufficient barrier against permeation of gases to increase the food and drink self-life [15]. Depositing a silicon dioxide film at the surface of packaging materials is currently substituting Al-coated polymers because of the transparent and microwaveable properties of silica films [18].

As a corrosion protective layer of metals [19] the use of silicon dioxide layer for certain metals and alloys on strategic applications such as power system [20] may open a discussion. Considering all the applications of these materials (p-Si, n-Si & $SiO_2$) and RF sputtering being one of the most effective growing techniques, in this work we tried to analyze several properties of the materials after RF sputtering according to the Taguchi design of experiments (DOE) [21, 22].

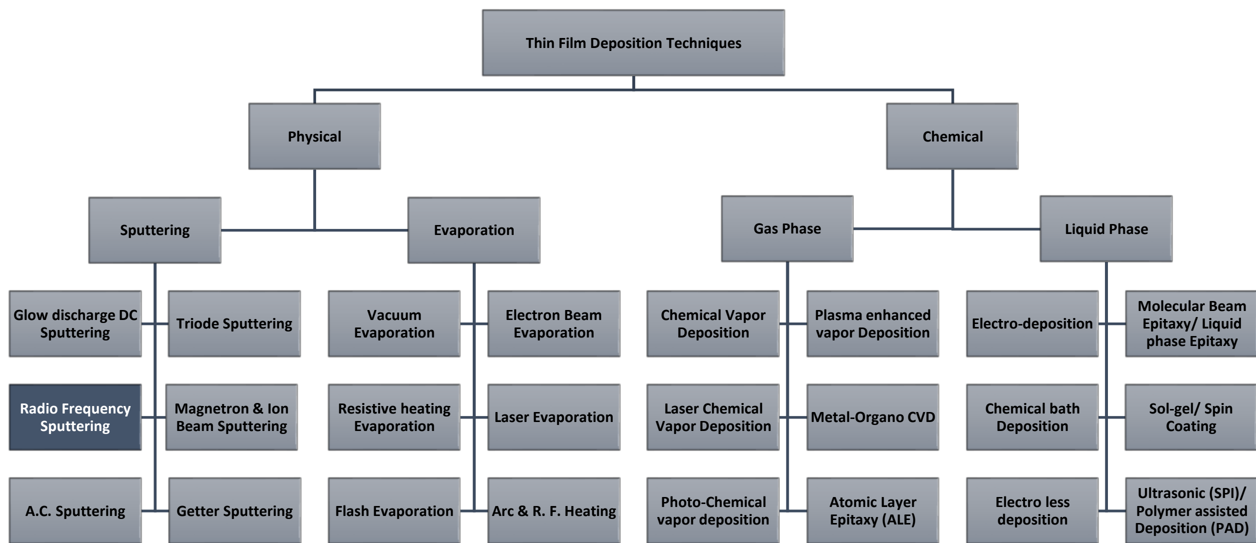


Figure 1: Classification of thin film deposition techniques

We also made an experimental design to observe the properties after deposition according to the Taguchi methods for SiO2. Taguchi analysis reduced the fabricating cycle for design and production, which decreased the cost and time [23]. The whole designing system was divided into three stages, where parameter design was the most significant one. The factors that affected the outputs were required for making the orthogonal array, and then experiments were conducted according to the orthogonal array. The goal was to obtain the best output by analyzing the experimental data obtained. Then conducting the confirmation runs at the optimal parameters, the best yield was found. For applying Taguchi design, factors that affect the outputs should be

identified at first from the literature. The most important factors during fabrication in RF sputtering system related to the outputs such as surface roughness, grain size and micro-strain in the grain boundaries are determined from the literature review. Factors that affect those outputs are mainly processing power, processing gas flow rate, and the chamber process pressure. Lots of articles reported some other factors [24-26] such as target to substrate distances, processing temperatures etc.

## 1.2 Magnetron sputtering

Magnetron sputtering is a high-rate vacuum coating technique for depositing metals, alloys, and compounds onto a wide range of materials with thicknesses up to millimeter. It exhibits several important advantages over other vacuum coating techniques, a property that led to the development of many commercial applications from microelectronic fabrication to simple decorative coatings. Magnetron sputtering is a widely used technique for thin film deposition. A simplified scheme of the magnetron is given in Fig.1.4. It is an abnormal glow discharge in the crossed electric and magnetic fields. Electrons emitted from the target due to argon bombardment are held in the magnetic “trap” near the target and ionize neutral argon atoms due to collisions [27]. Charged ions of the working gas accelerate to the target and eject atoms of the sputtered material, for example metal, by momentum transfer. Metal atoms flow through the magnetic field and settle on the substrate which is in front of the target. A high concentration of electrons near the target results in a high probability of ionization of the working gas, usually Ar [28]. A high ionization of the plasma allows to operate at low pressures and high discharge currents resulting in a significant deposition rate of the film [29, 30]. Also, due to advantages of magnetron sputtering such as preparation of high-quality defect-free films [6], high deposition rate [29, 30], easy control of elemental composition and structure of the growing film [31], it is

widely used in various industrial applications such as optical coatings [32], hard coatings for cutting tools [33-36], decorative coatings [37], microelectronics [38], solar cells [39] and so on. It is important to note that magnetron sputtering can in addition be easily modified, for example by [34]:

1) Increasing the degree of ionization (hollow cathode, additional RF source)
2) Modification of the voltage waveform (DC, AC, RF, DC pulsed, HiPIMS)
3) Introduction of the reactive gas into the discharge
4) Modification of the magnetic field (conventional or unbalanced magnetron, mirror or closed magnetic field configuration of dual magnetron)
5) Co-sputtering with other deposition techniques like ECR or CV

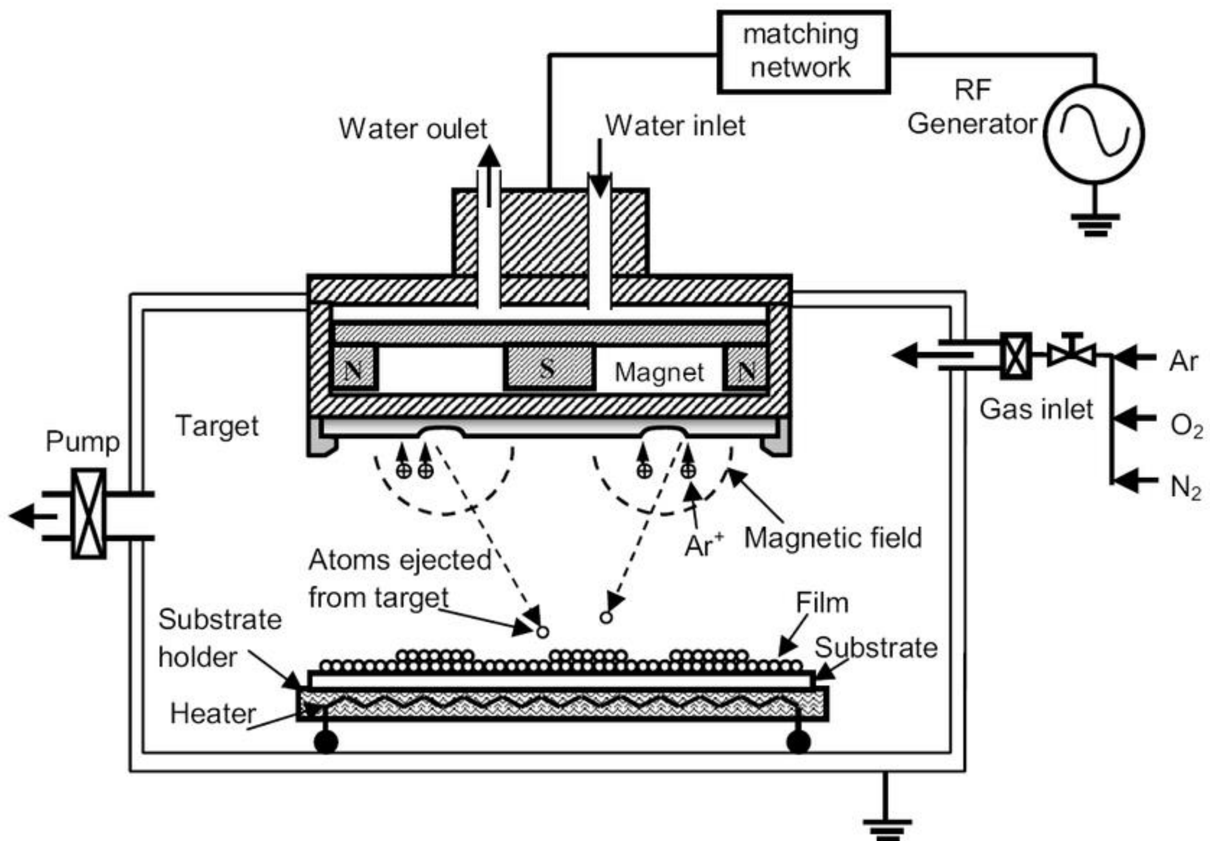


Figure 2: RF magnetron sputtering system main chamber [40].

### 1.2.1 Reactive sputtering

Magnetron sputtering can be divided onto non-reactive and reactive sputtering. In the first case, the films produced by sputtering of an elemental target in a noble gas atmosphere. The second way is to introduce a certain amount of the reactive gas, such as oxygen or nitrogen, in addition to the working gas. Reactive sputtering is a fine-tuned and flexible process which allows to produce oxides, nitrides, carbides, oxynitrides and other materials. In the case of non-conducting materials, for example AlN, it is possible to produce it from a pure metal Al target without using a complex RF sputtering. Unfortunately, the deposition rate in the reactive sputtering is lower than the rate for a pure metal deposition due to the several reasons [34, 41]:

1. Sputtering yield for a compound is lower than the corresponding for metal $\gamma(Metal) > \gamma(compound)$, e.g., $\gamma(Ti) > \gamma(TiN)$

2. Reactive gases typically have low atomic mass; therefore, they are highly ineffective in sputtering.
3. Decrease of the magnetron discharge voltage due to replacing of pure metal by its compound, for example Ti replaced by TiN.

This reduction follows from the phenomenon called the target poisoning. Chemical reactions and formation of the compound occurs on the surfaces of the substrate and the target [41].

## 1.3 Principle of plasma discharges

Plasma is an assembly of free charged particles (ionized atoms/molecules and electrons) moving in random directions produced when the atoms in a gas become ionized (Fig. 1.1a). It is an electrically conducting medium in which there are roughly equal numbers of positively and

negatively charged particles. Sometimes referred to as the fourth stated of matter, distinct from the solid, liquid, and gaseous states. Ions and electrons are produced in the gas phase when highly energized electrons or photons collide with the neutral atoms and molecules(electron-impact ionization or photoionization). There are various ways to supply the necessary energy for plasma generation to a neutral gas. These heated electrons have high enough kinetic energy and high possibility to ionize atoms during collisions. The ratio between charged and neutral particles in the plasma discharge is called the degree of ionization and is very important in the case of plasma deposition process [28].

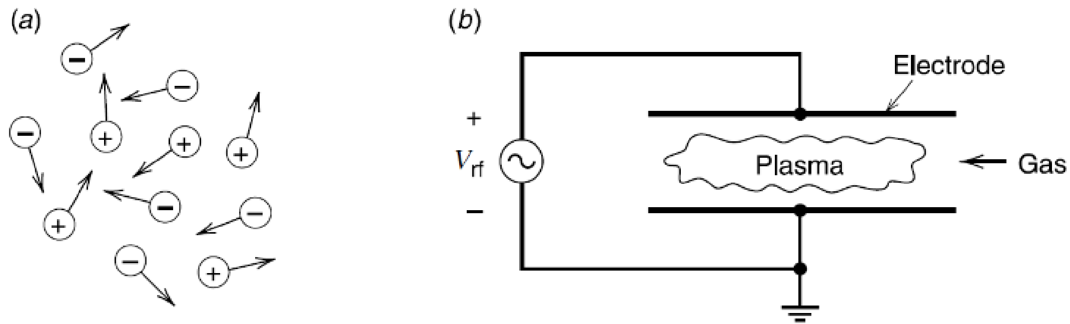


Figure 3: Scheme of a simple DC electrical discharge [28]

Fig. 2 shows a simple electrical discharge. It consists of two electrodes and a power source. Upon application of a dc voltage between the electrodes a discharge is formed after the breakdown of the working gas. Electrons emitted from the cathode are accelerated to the anode and generate positively charged ions by collisions with heavy particles. These heavy ions flow to the cathode and collide with its surface with sputtering of cathode material. Also, these collisions are the source of secondary electrons. These secondary electrons play an important role in the gas ionization mechanism, described by John Townsend. His equation shows his criteria of the transition from a nonstationary to a self-sustaining discharge:

$$\gamma e^{\alpha d} = 1 \quad 1.1$$

Here:

$\gamma =$ Townsend coefficient of secondary emission

$\alpha =$ Townsend coefficient of ionization

$d =$ Distance between cathode and anode

According to this formula, a self-sustaining discharge arises when each emitted electron creates 1 secondary electron which takes over its function. Both coefficients $\gamma$ and $\alpha$ are strongly dependent on the working pressure and distance between the electrodes. This dependence was experimentally determined by Friedrich Paschen, who obtained the breaking voltage as a function of the gas pressure, distance between two electrodes and the type of gas. Fig.1.2 shows typical Paschen curves for noble gases.

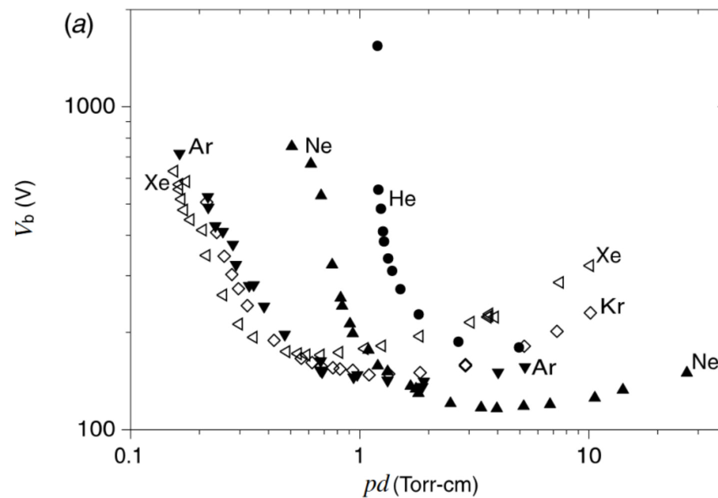


Figure 4: Paschen curves for noble gases [28]

The current-voltage characteristic of a dc discharge can be divided onto several regimes, which are characterized by a completely different degree of ionization and energies of electrons and ions. Typical I-V characteristic is shown in Figure 4. Three characteristic regimes can be determined:

1. Townsend discharge or dark discharge where the current increases with only little increase of the voltage and the free electrons carry enough energy for further ionization.
2. Glow discharge. In this regime the voltage drops and the current increases to the milliampere range. At low current, the voltage is current-independent. At higher current, the normal glow turns into the abnormal glow and the voltage gradually increases.
3. Arc discharge. In this regime the current achieves the ampere range, and the voltage significantly drops with increasing of current.

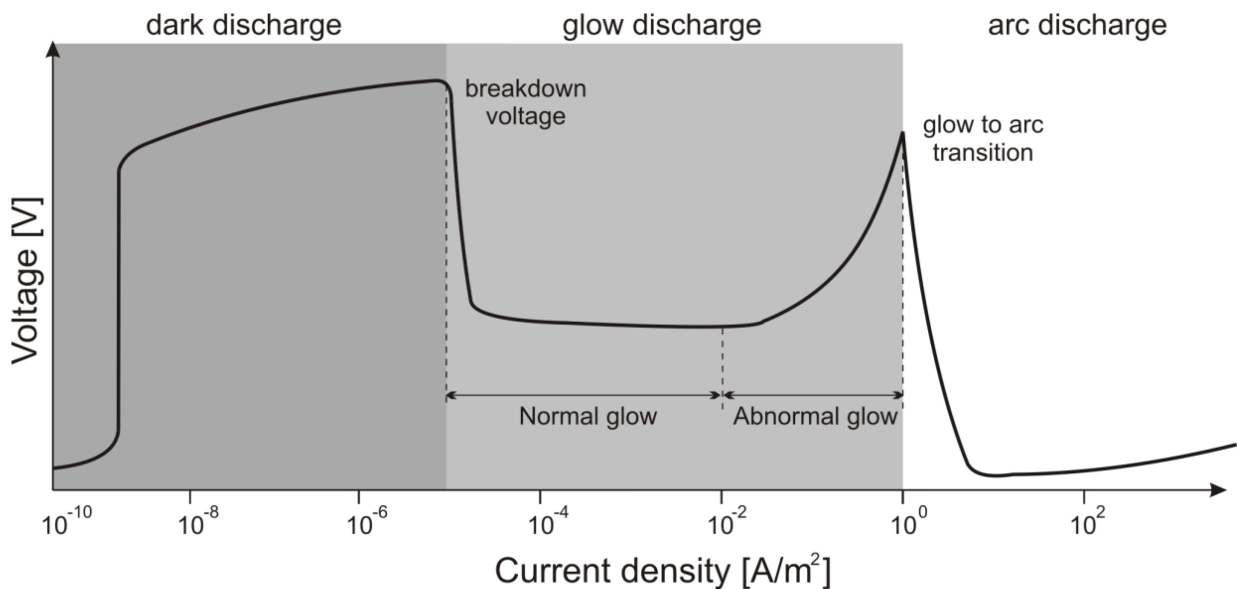


Figure 5: I-V characteristics of DC discharge

### 1.4 Ion Bombardment to the surface

The physical sputtering is a process whereby particles are ejected from a solid target material due to bombardment of the target by energetic particles [28]. These energetic particles, usually ions of noble gas, are accelerated by electrical field and transfer the momentum to the atoms of target material by collisions [27, 28]. Sputter deposition of thin films as a term then characterizes the process where a surface being sputtered serves as the source of the deposited

material. The sputtered particles are transported from the target to the substrate typically without collisions in a plasma discharge [28]. Probability to sputter an atom from the surface of the target depends on the energy of the incident particle and its mass.

Another important parameter is the sputtering yield which is the ratio of sputtered particles to bombarded particles and characterizes the sputtering efficiency. Sputtering yield depends on several parameters such as the nature and strength of bonds in the target material, target elemental composition and the angle of flux of bombarded particles. It is relatively insensitive to the target temperature [29]. Sputtering yields of elements or compounds are determined experimentally. It is characterized by the erosion rate, which is determined as:

$$R = \frac{\gamma J}{ne} \text{ (cm/min)} \qquad 1.2$$

Here,

$J$ = ion current density in mA/cm2,

$\gamma =$ sputtering yield in atoms/ion,

$e =$ elemental charge

$n =$ density of the target material in g/cm3

### 1.4.1 Effects of Ion bombardment to surface

When a solid surface is hit by an ion following happens. And during ion bombardment, the solid surface is called the target.

- The ion can be reflected and can be neutralized immediately afterwards.
- The ion bombardment can eject an electron from the target, and a secondary electron is created.

- The ion can penetrate the target which is known as ion implantation. This process is widely employed in IC technology for selectively doping silicon wafers.
- The ion can cause structural changes in the target material results in interstitial defects and major lattice defects which can provoke changes in the target composition.
- Finally, the ion impact can originate a series of collision among the target atoms, leading to the ejection of one of these atoms. This election process is called sputtering.

Considering all these physics behind the processing, factors to be considered for thin films characterization are determined and outputs are analyzed.

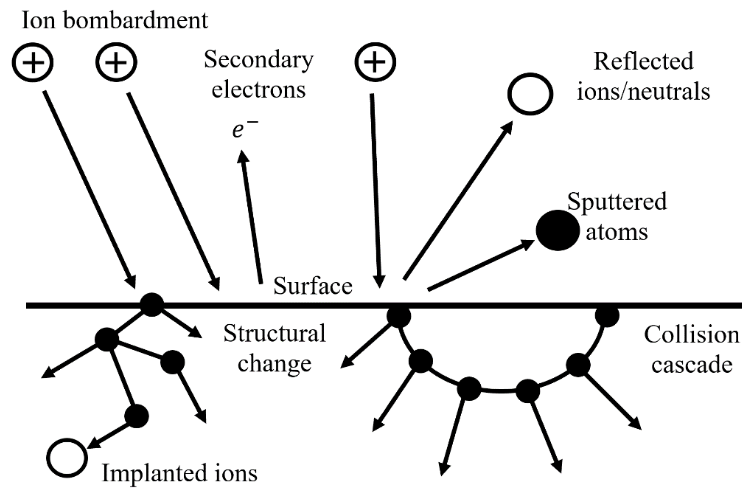


Figure 6: Ion bombardment effect on the surface

## 1.5 Thesis Outline

This thesis is based on the following four steps.

1. Finding the impact of process parameters during RF sputtering of p-Si, n-Si & SiO2 thin films.

2. Analyzing various output properties such as surface roughness, micro stress and grain size using XRD, AFM and profilometer.
3. Creating mathematical models by performing regression analysis after analyzing the data as there is no model found for predicting output characteristics as a function of Ar flow rate, Ar pressure, RF power, and process temperature.
4. Performing signal to noise ratio (S/N) and variance analysis (ANOVA) to observe the contribution of each parameter to the outputs.

CHAPTER II

METHODOLOGY

## 2.1 FABRICATION

Characterization of three materials (p-Si, n-Si & SiO2) were divided into three different parts. First, it started with the fabrication of the thin films. Second, characterization in different characterizing tools and data acquisition. Third, analysis of the date and mathematical model making. The three steps are described by figure 7, figure 12 and figure 18.

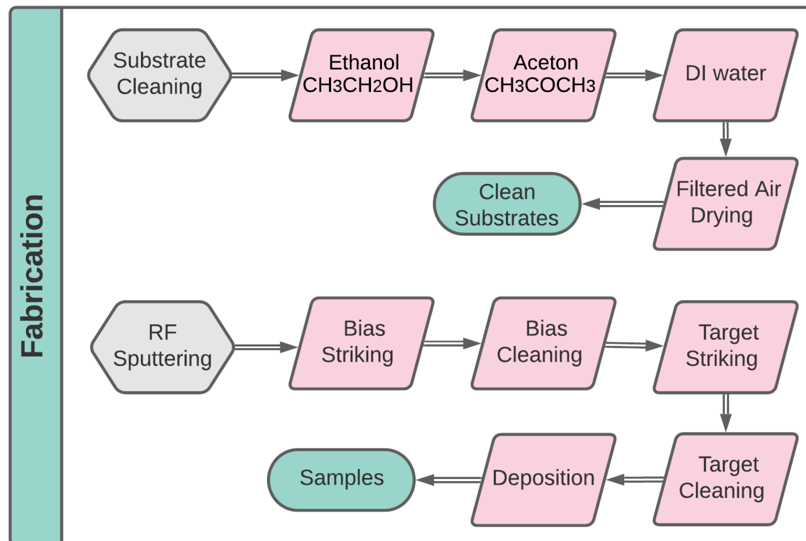


Figure 7: Thin films fabrication steps

### 2.1.1 Cutting and Cleaning

We used Silicon wafer of fixed planes and lines (Figure 8). After cutting into pieces fabrication started with the cleaning process. Proper cleaning and preparation of substrate before

the deposition is critical to the success of the sample preparation. Proper cleaning and surface preparation conditions are followed before using the PVD system. Failure to adhere to these requirements can cause adhesion loss and, therefore, reduce the samples' durability and performance level. All substrate surfaces were considered contaminated and cleaned before the application in the RF magnetron sputtering system.

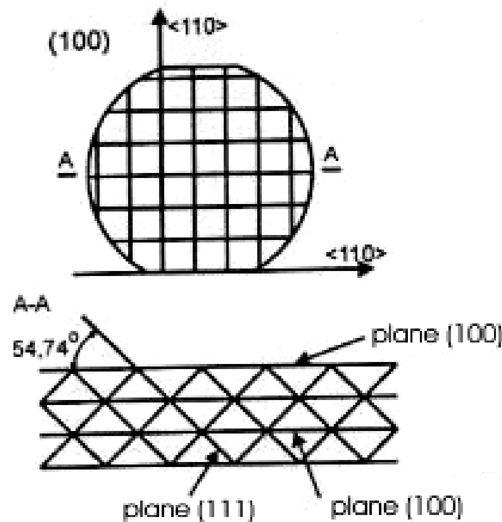


Figure 8: Silicon wafer and plane

In step one, substrate samples were cleaned by deionized water (figure 9(a)). When water is deionized, it draws in other minerals and elements, such as those found in dirt and contaminants. Since there are no minerals in deionized water, it leaves behind no residue, spots, or stains on surfaces. Next, the samples were dried in filtered air (figure 9(b)). When dried in the air, substrates are prevented from rusting and corrosion caused by redundant moisture. It also helped to get rid of water that can affect adherence. Then ethanol ($CH_3CH_2OH$) solvent (figure 9(c)) was used with the help of a vortex micromixer (figure 9(e)). Ethanol is a comparatively cheap solvent and can dissolve any undesirable organic substances accumulated on the surfaces to clean it. Next, acetone ($CH_3COCH_3$) (figure 9(d))was used because acetone is an excellent

solvent; it is a very polar substance that dissolves almost all organic compounds, which is critical when cleaning. At last, DI water was used to clean the samples and dried them in the filtered air.

Figure 9: Cleaning steps (a)Di water (b) filtered air (c) ethanol (d) acetone (e) micromixer.

### 2.1.2 RF Magnetron Sputtering

The as-cleaned silicon substrates was put to the main chamber of ATC ORION 5 UHV RF magnetron sputtering system (figure 10) and different processing steps were employed. This PVD system operates with Direct Current (DC) and Radio Frequency (RF) of 13.56 MHz at low pressure <20mT and erodes atoms from a planar target with 99.9% pure targets hold by a gun namely DC/RF gun. To remove impurities, a pre-sputtering process is employed where the turbo pump removes all the foreign particles presented in the deposition chamber. A series of steps are followed, depicted in Table 1. In bias striking step, the deposition environment are ignited to

create plasma, then bias cleaning to clean the substrate and the main chamber. To prepare the target for sputtering target striking is conducted and to remove the oxide layer from the target cleaning is operated as a pre-deposition. These four steps prepare the main chamber to be a perfect environment for the experiment.

Table 1: Pre-deposition Steps for p-Si and n-Si at 25$^{o}$C temperature

| | Bias Strike | Bias Clean | Target Strike | Target Clean |
|---|---|---|---|---|
| Pressure | 30 mT | 3 mT | 30 mT | 10 mT |
| Gas (Ar) | 15 sccm | 15 sccm | 15 sccm | 5 sccm |
| Power (RF) | 25 watts | 50 watts | 100 watts | 100 watts |
| Time | 10 sec | 20 sec | 10 sec | 30 min |

Table 2: Pre-deposition Steps for $SiO_2$ at 25$^{o}$C temperature

| | Bias Strike | Bias Clean | Target Strike | Target Clean |
|---|---|---|---|---|
| Pressure | 30 mT | 3 mT | 30 mT | 5 mT |
| Gas (Ar) | 15 sccm | 15 sccm | 15 sccm | 5 sccm |
| Power (RF) | 25 watts | 50 watts | 75 watts | 100 watts |
| Time | 10 sec | 20 sec | 10 sec | 10 min |

**System Configuration:**

Max power: 300 w (RF), 750 w (DC)

Max voltage: 1000 V

Max current: 1000mA

Temperature range : (25 – 850) Degree Celsius

Ar flow rate limit : 20 sccm

$N_2$ flow rate limit: 20 sccm

Figure 10: RF sputtering system (Sputtering system lab, UTRGV)

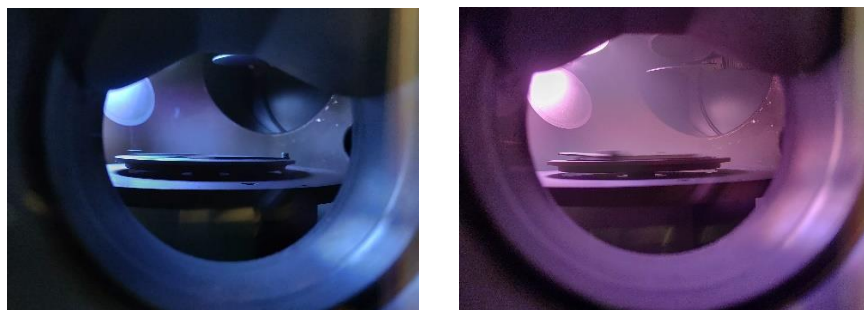

Figure 11: Plasma creation for process gas (a) Ar (b) $N_2$

## 2.2 MORPHOLOGICAL AND PHYSICAL CHARACTERIZATION

Five types of characterizing instruments are employed to observe the as-grown surface morphology and the crystallography.

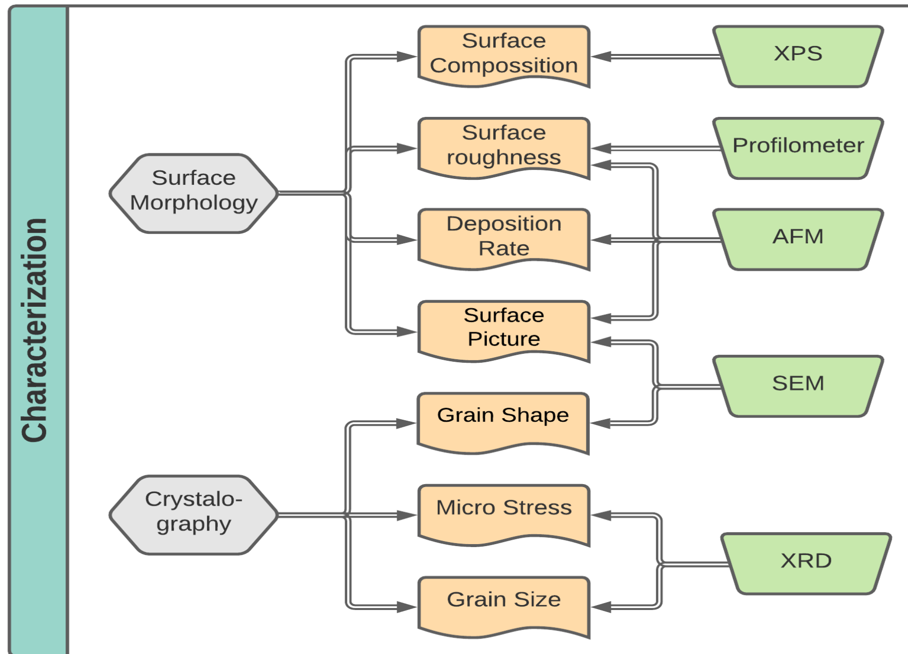


Figure 12: Surface morphology and crystallography steps

### 2.2.1 X-Ray Diffraction

Samples were analyzed using Rigaku miniflex benchtop powder x-ray diffractometer with Cu K Alpha radiation with x-ray source of $\lambda$= 1.5406 Å, 30 kV and 15 mA (figure 15). The operation of XRD is explained in more details in next chapter. This configuration is dedicated for powder experiments but is also possible to get the analysis of the thin films by rotating the specimens and trying different positions until the elemental picks are identified according to Bragg's law (figure 14). The scanning was operated from 10$^o$ to 90$^o$ for all the samples because a pre-scanning within the whole range confirmed the range of all the peaks. The scanning time was 2 sec for each angle with the stepping size of 0.1$^o$ each.

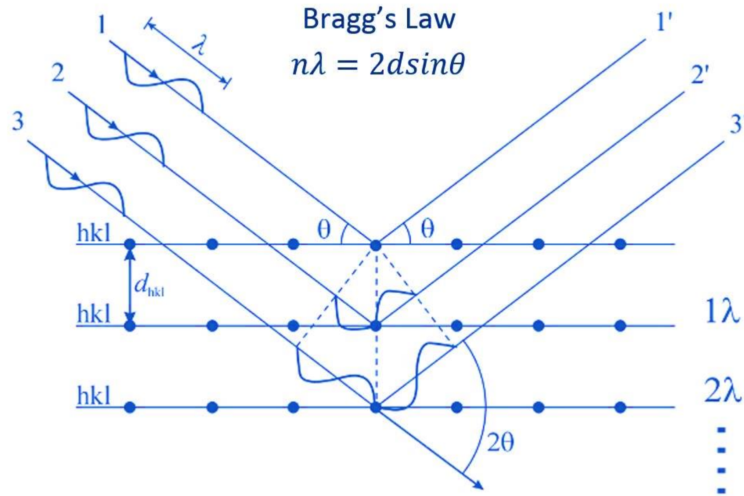


Figure 13: Application of Bragg's law in XRD

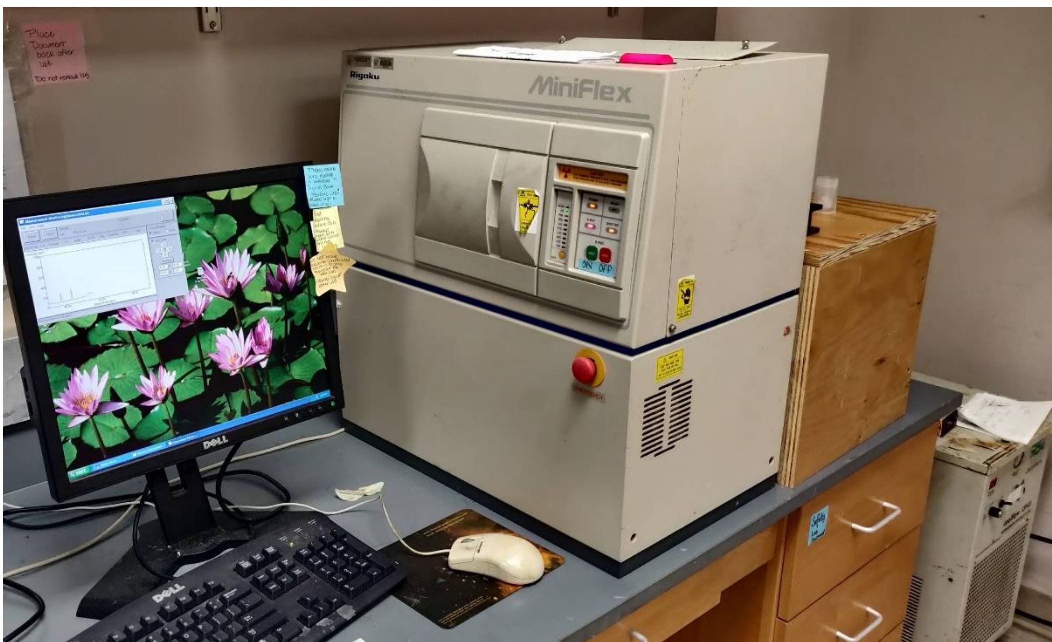


Figure 14: Rigaku miniflex benchtop powder x-ray diffractometer

### 2.2.2 Profilometer

To inspect the surface roughness Marsurf 300c profilometer (figure 16) and atomic force microscope were employed.

Figure 15: Marsurf 300c profilometer

### 2.2.3 Atomic force Microscope

The topography namely the surface images and thickness were observed using a tapping mode Veeco Dimension 3100 AFM. The basic configuration of AFM is shown in figure 17.

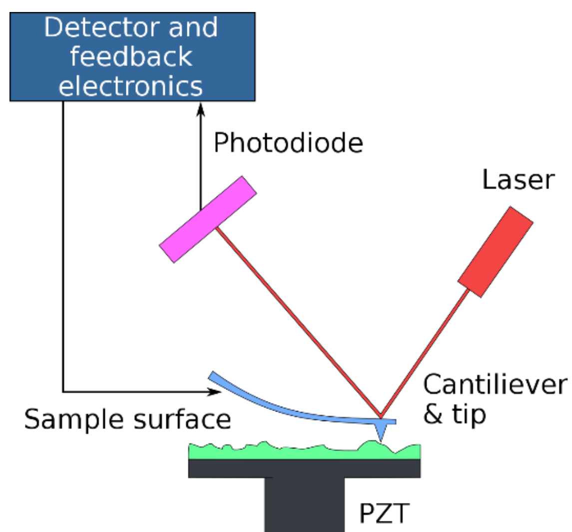


Figure 16: AFM block diagram

## 2.3 STATISTICAL ANALYSIS

The analysis started with the Taguchi Design of Experiment. Taguchi design of experiments (DOE) (figure 2-b) is a complete factorial design that identifies all combinations for the given factors [21, 22]. Since a complete factorial design requires too many experiments, a partial factorial design was performed to select a small set in all experimental combinations. Three sets of RF power (100, 150 & 200W), pressure (10, 15 & 20 mTorr) and Ar gas flow rate (5, 10 & 15 sccm) were chosen as process parameters for sputtering and 3 level Taguchi design of experiment was applied to create an $L^9$ $(3^3)$ orthogonal array which is shown in Table 1.

Table 3: Selective sputtering parameters and their levels

| Level | Sputtering parameter | 1 | 2 | 3 |
|---|---|---|---|---|
| A | RF Power (W) | 100 | 150 | 200 |
| B | Working Pressure (mTorr) | 10 | 15 | 20 |
| C | Ar flow rate (sccm) | 5 | 10 | 15 |

### 2.3.1 Signal to Noise Ratio (S/N) Analysis

Signal to noise ratio is the most important analysis of Taguchi design [22]. The output characteristics are classified into either desirable or undesirable effects. Desirable effects of output characteristics are known as “Signal” and the undesirable effects are called “Noise”. There are three types of performance characteristics in the analysis of the Signal to Noise (S/N) ratio, which are known as smaller the better, higher the better, and nominal the better. S/N ratio is used to find out the optimal condition of the control parameters [42]. Signals are the controllable process parameters whereas noise is something we have no control during

production but can be controlled during experimentation. In this experiment the goal is to minimize the surface roughness, and the micro-strain and to maximize the grain size. Therefore, the smaller the better S/N ratio has been applied for surface roughness, and micro-strain and the larger the better S/N ratio has been applied for grain size. The smaller the better S/N ratio is calculated as follows-

$$S/N = -10\log_{10}\left[\frac{1}{n}\left(\sum_{i=1}^{n} y_i^2\right)\right] \qquad 2.1$$

The larger the better S/N ratio is calculated as follows-

$$S/N = -10\log_{10}\left[\frac{1}{n}\left(\sum_{i=1}^{n} \frac{1}{y_i^2}\right)\right] \qquad 2.2$$

Here, $y_i$ is the $i^{th}$ measurement values in a run and n is the number of measurements in each trial in the factor level combination. The optimal level of process parameters always corresponds to the highest S/N ratio when the optimization is performed based on a single performance characteristic. However, the optimization of multiple performance characteristics differs from that of single performance characteristic. The higher S/N ratio for one response characteristic may correspond to the lower S/N ratio for another response characteristic. Therefore, the optimization of multiple performance characteristics may require the overall evaluation of the S/N ratio.

### 2.3.2 Analysis of Variance (ANOVA)

Analysis of variance (ANOVA) was performed to find out which sputtering parameters had statistically significant effect over a particular output. The following equations were used for ANOVA and F-test of the experimental data.

$$S_{mean} = \frac{(\sum x_i)^2}{n} \qquad S_{TV} = \sum x_i^2 - S_{mean}$$

$$S_p = \frac{\left(\sum x_p^2\right)^2}{n_{rpt}} - S_{mean} \qquad S_{Error} = S_{TV} - \sum S_p \qquad 2.3$$

$$V_p = \frac{S_p}{f_p} \qquad F = \frac{V_P}{V_{Error}}$$

Where, N was total number of experiments, $x_i$ was the output of each experiment, $S_{mean}$ was the sum of squares due to the means, $S_{TV}$ was the sum of square due to the total variation, $S_p$ was the sum of square due to a parameter, $x_p$ was the sum of the ith level of a parameter (i=1, 2, 3), fp was the degree of freedom of a parameter, $V_p$ was the variance of a parameter and F was the test value of a parameter. An optimal combination of the process parameters was predicted from S/N ratio and ANOVA analysis [22, 43].

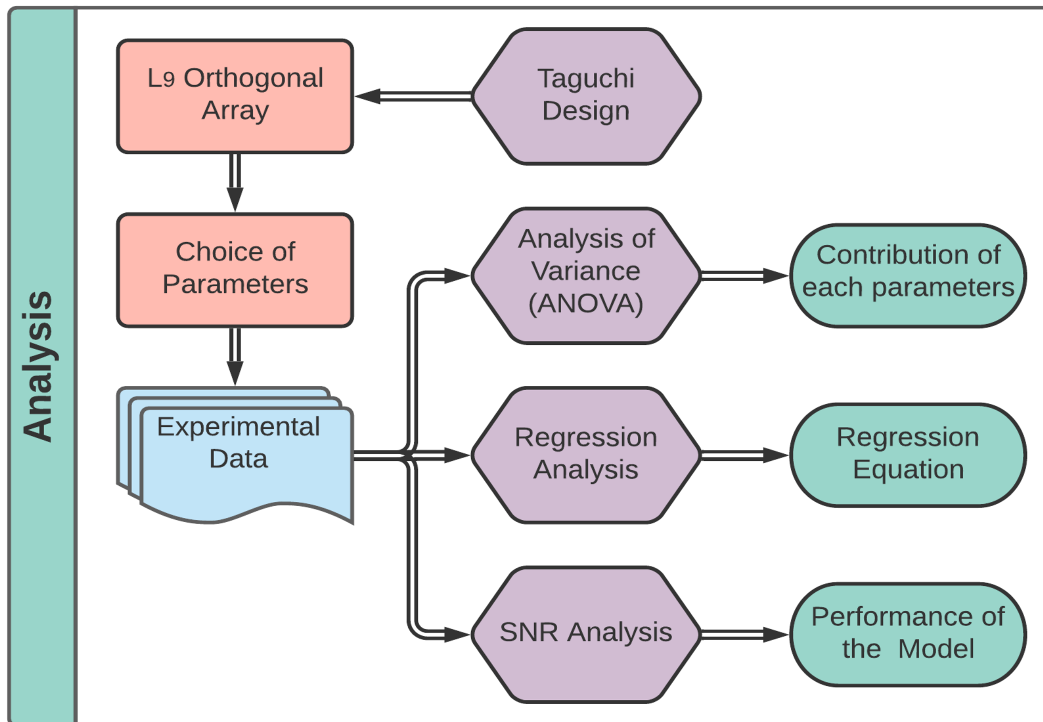


Figure 17: Taguchi analysis steps

### 2.3.3 Terms in the Statistical Analysis

**The standard error of the regression (S-value):** S represents the average distance that the observed values fall from the regression line.

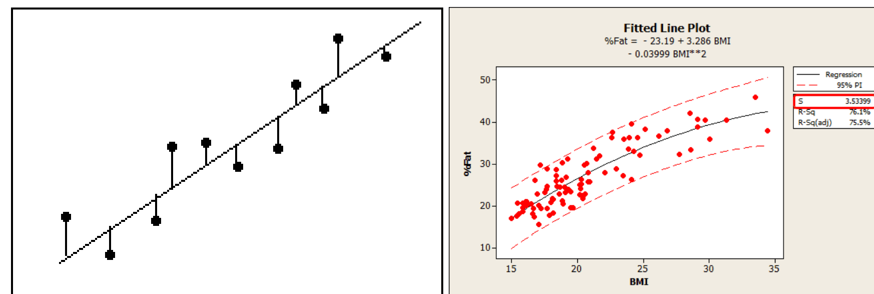


Figure 18:Standard error (S) of regression

Smaller value of S is better because it indicates that the observations are closer to the fitted line.

The value of S is large = Data are spread out from the mean

The value of S is small = Data are very close to the mean

**The linear correlation coefficient ($R^2$):** R-squared ($R^2$) is a statistical measure that represents the proportion of the variance for a dependent variable that is explained by an independent variable or variables in a regression model. Whereas correlation explains the strength of the relationship between an independent and dependent variable, R-squared explains to what extent the variance of one variable explains the variance of the second variable.

The value of $R^2$ is large = Data are closely varying from the mean

The value of $R^2$ is small = Data are largely varying from the mean

**P-value:** Mathematically, the p-value is calculated using integral calculus from the area under the probability distribution curve for all values of statistics that are at least as far from the reference value as the observed value is, relative to the total area under the probability

distribution curve. In a nutshell, the greater the difference between two observed values, the less likely it is that the difference is due to simple random chance, and this is reflected by a lower p-value.

P-Value is a probability number from 0 to 1.

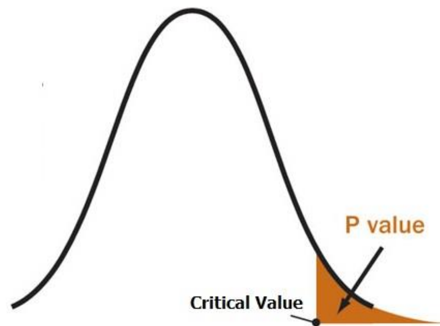


Figure 19: Calculation of P-Value

High P values = Your data are likely with a true null hypothesis.

Low P values = Your data are unlikely with a true null hypothesis.

A small p ($\leq 0.05$), reject the null hypothesis. This is strong evidence that the null hypothesis is invalid. And a large p ($> 0.05$) means the alternate hypothesis is weak, so you do not reject the null.

My null hypothesis was there was no contribution of power for surface roughness.

**How to get P-Value:** From Z-Test, t-Test, and many other tests you will get a value and you can find P-value for that corresponding (Z-Test or t-Test) value from the P-Value table. It is normally available in statistics book or software.

**F-value:** F = Variation between sample means / Variation within the samples

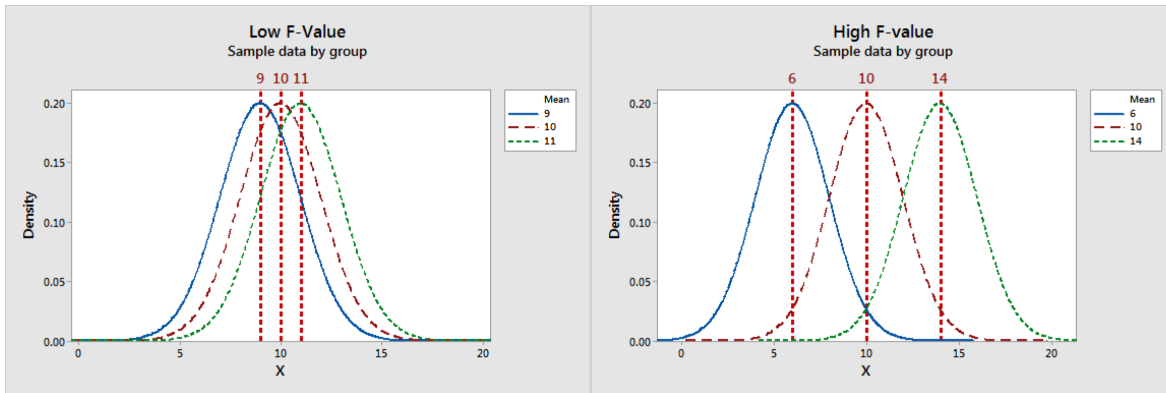


Figure 20: F- Value comparison

High F-value = Reject the null hypothesis

Low F-value = Accept the null hypothesis (i.e., all the sample mean are equal).

CHAPTER III

MESUREMENTS & CHARACTERIZATION

## 3.1 X-RAY DIFFRACTION (XRD)

X-ray diffraction (XRD) is one of most important non-destructive methods of structural characterization. In a typical XRD measurement of a thin film, incident X-rays impinge on the film and are diffracted into a range of angles. These diffracted X-rays (forming Bragg peaks) are then collected. The pattern of intensity versus angle is then the diffraction (or reciprocal space) pattern of the film.

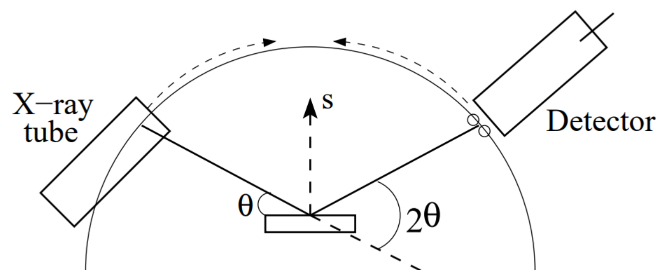


Figure 21: Basic structure of XRD machine

XRD measurements can extract information such as presented phases, crystallite size, lattice strain, crystallite orientations and defects (stacking faults, strain distribution). X-ray scattering from thin films can be weak, especially if the film structure is disordered and can be strong when order is present. Diffraction occurs from periodic structures that are illuminated with light of a wavelength comparable to the spacing of the objects. Since X-rays have wavelengths of ~1 Å,

they will diffract from objects that have periodic spacings on the order of Angstroms, e.g., atoms in a crystal.

Diffraction occurs through constructive interference, when the path difference between two rays of light is equal to an integer multiple of the wavelength (Figure. 1.1). This results in the Bragg equation:

$$2d \sin\theta = n\lambda \qquad 3.1$$

where $\theta$ is half of the scattering angle, $2\theta$; $\lambda$ is the wavelength of the X-ray light, $n$ is an integer, and $d$ is the so-called 'd-spacing' between the diffracting planes.

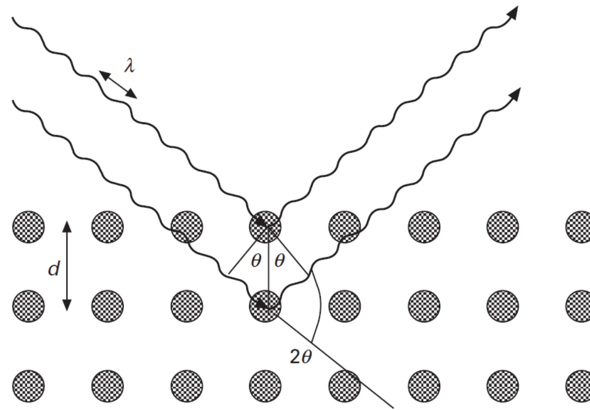


Figure 22: Diffraction from a periodic arrangement of atoms satisfies the Bragg equation.

While a diffraction grating has periodicity in one dimension, crystals have periodicity in three dimensions. They are characterized by symmetry relations between the atoms. Observing diffraction peaks:

diffraction occurs when there is constructive interference from X-rays scattering from planes of atoms (the crystal planes). The d-spacing is the distance between these crystal planes in real space. The smaller the d-spacing, the higher the diffracted angle, 2*q*. The crystal planes – and the diffraction peaks that arise from them – are identified according to their miller indices (*hkl*).

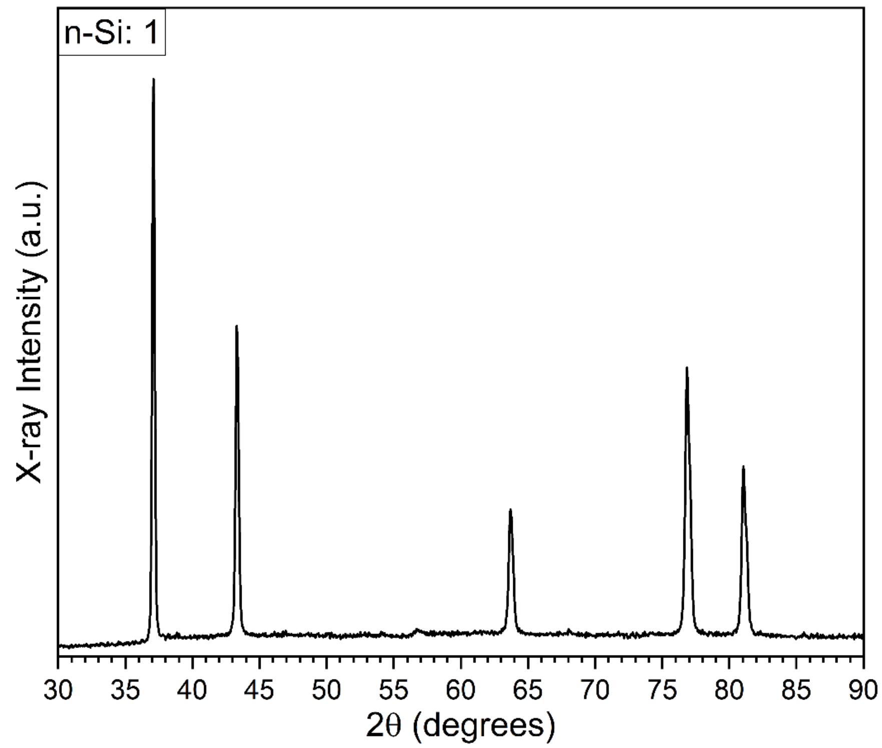


Figure 23(a): XRD pattern of RF sputtered n-Si (sample 1)

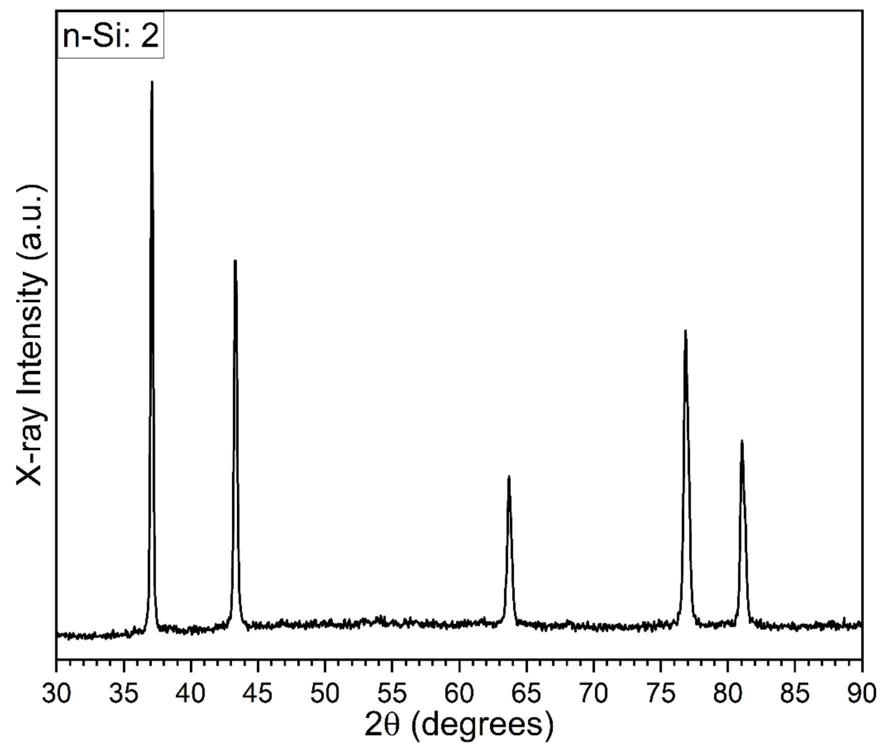


Figure 23(b): XRD pattern of RF sputtered n-Si (sample 2)

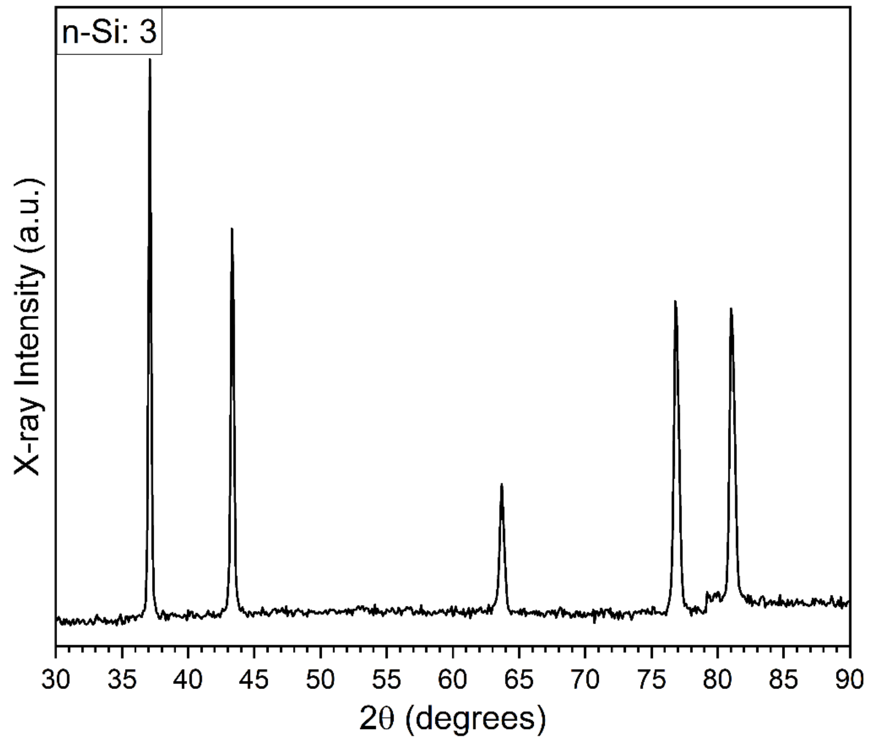


Figure 23(c): XRD pattern of RF sputtered n-Si (sample 3)

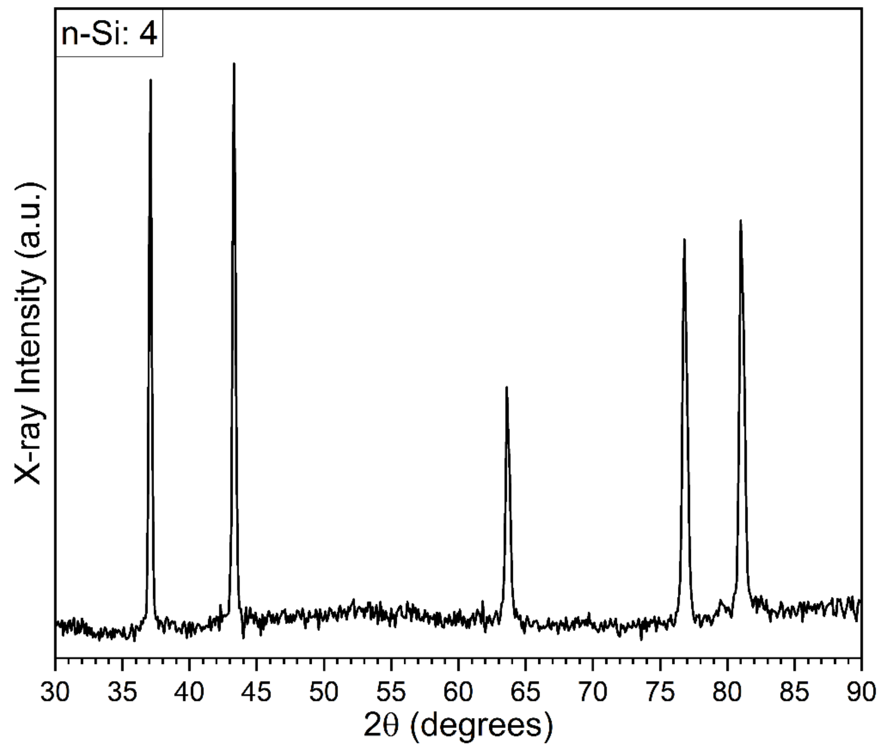


Figure 23(d): XRD pattern of RF sputtered n-Si (sample 4)

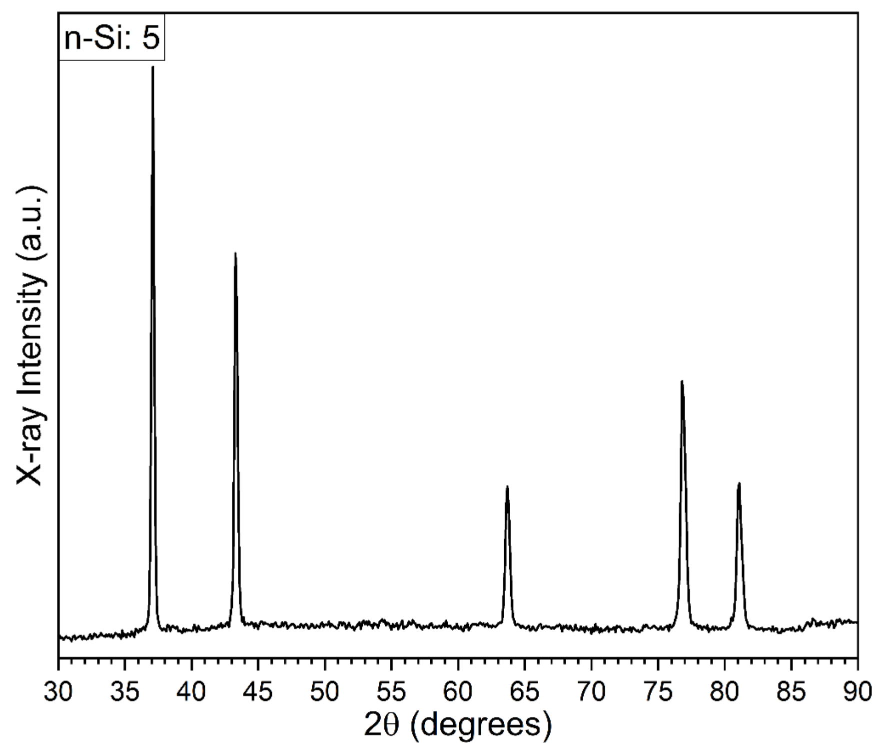


Figure 23(e): XRD pattern of RF sputtered n-Si (sample 5)

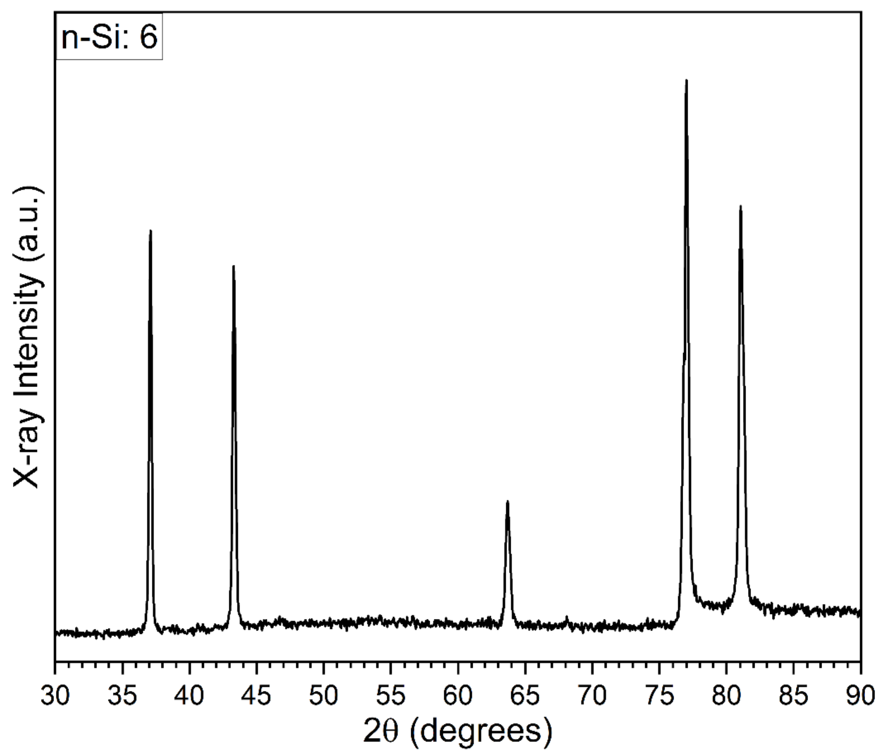


Figure 23(f): XRD pattern of RF sputtered n-Si (sample 6)

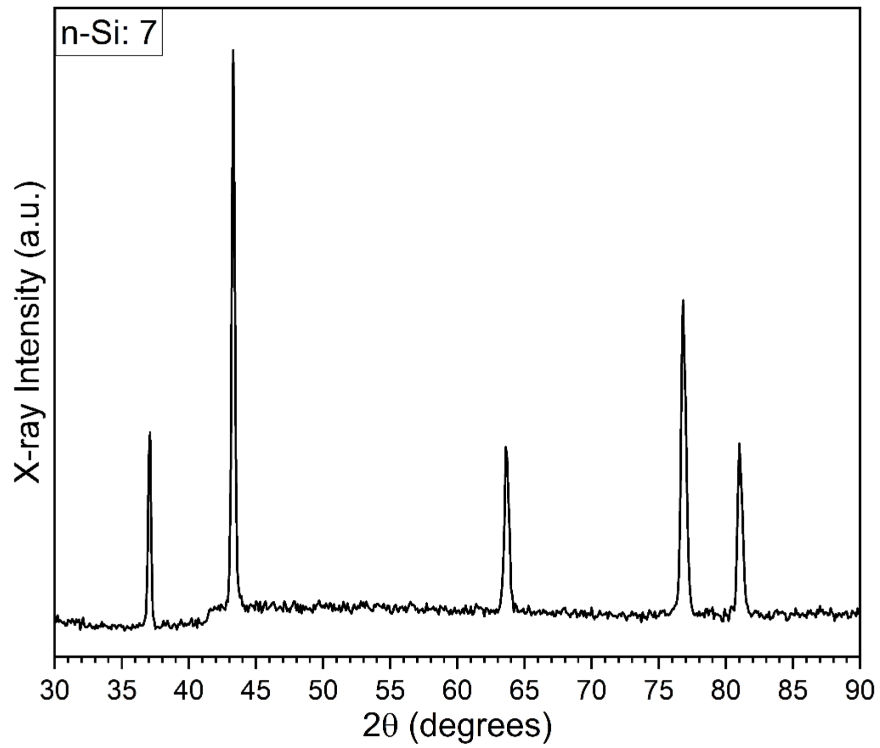


Figure 23(g): XRD pattern of RF sputtered n-Si (sample 7)

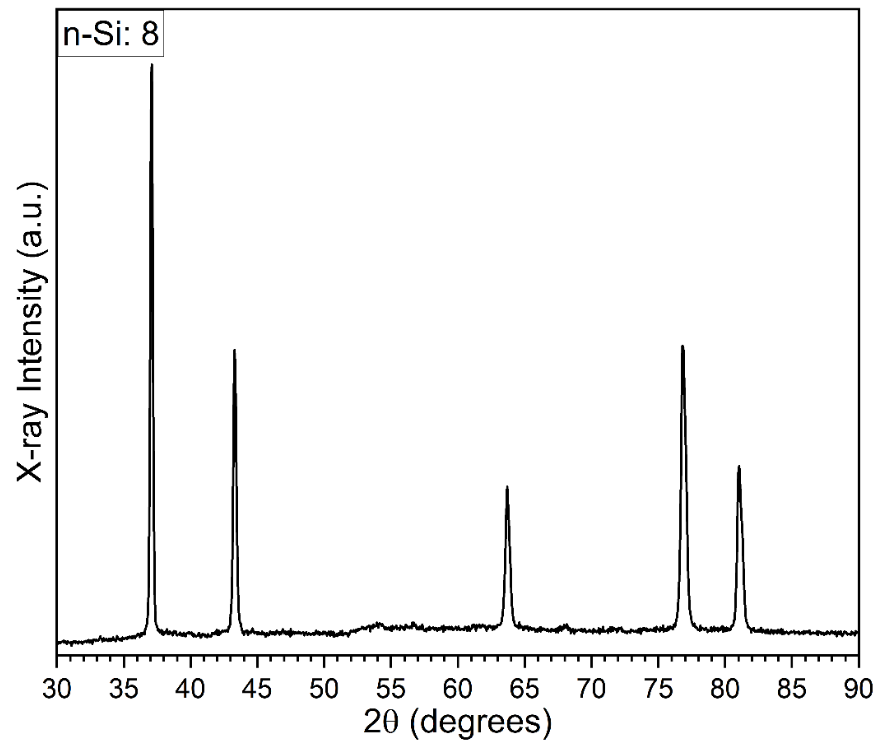


Figure 23(h): XRD pattern of RF sputtered n-Si (sample 8)

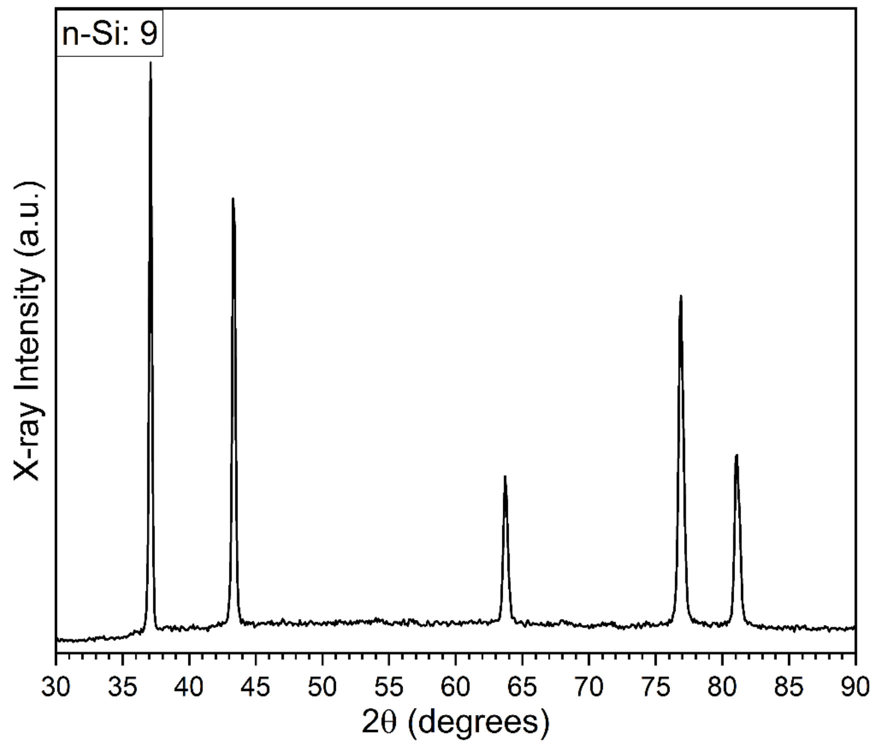


Figure 23(i): XRD pattern of RF sputtered n-Si (sample 9)

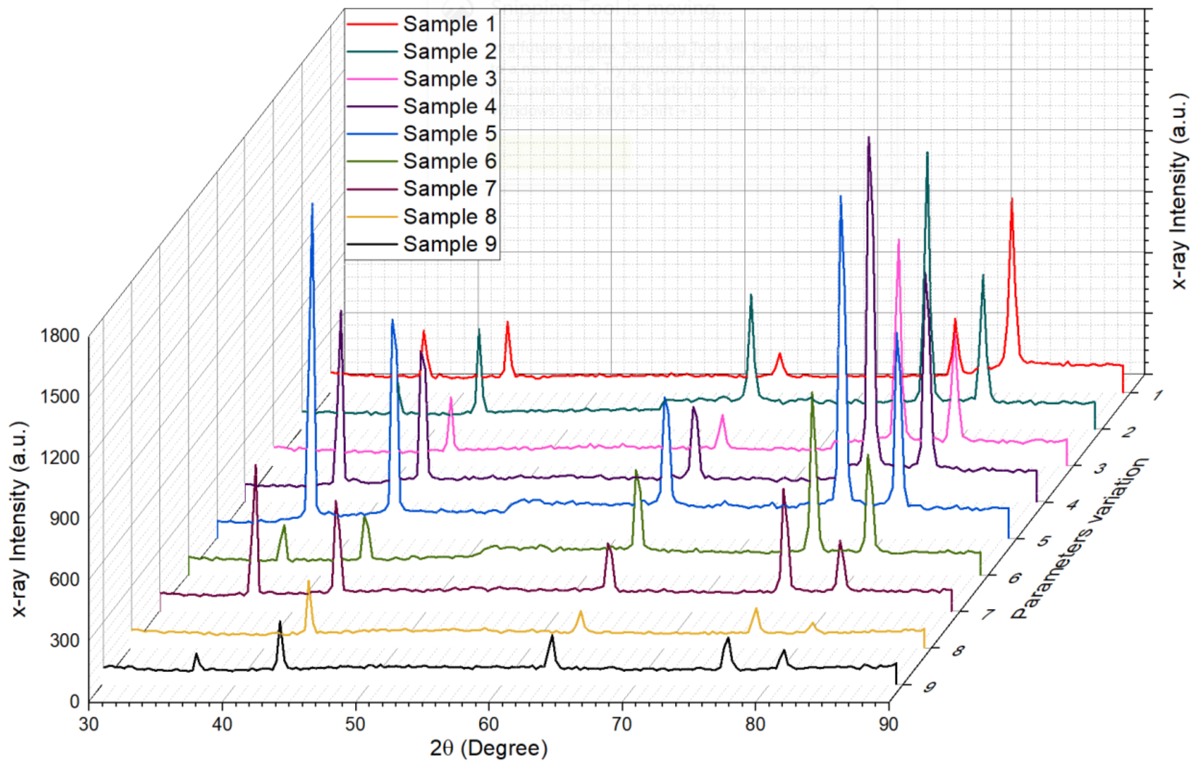


Figure 24: X-ray intensity pattern of 9 p-Si samples

### 3.1.1 Crystallite size Scherrer method:

A simple and well-known expression for obtaining a measure of the crystallite size from X-ray diffraction peaks is that of the Scherrer equation. Peaks from the x-ray diffraction gets broadens in the nanocrystals due to the crystalline size effect and intrinsic strain effect and this peak broadening normally consists of two parts namely physical broadening and instrumental broadening [44-47]. This instrumental broadening can be corrected using the following relation,

$$\beta_d^2 = \beta_m^2 - \beta_i^2 \qquad 3.2$$

Where, $\beta_m$ is the measured broadening, $\beta_i$ is the instrumental broadening and $\beta_d$ is the corrected broadening. Here, for position calibration and instrumental broadening calculation, crystalline silicon has been used as a standard reference material. Bothe the instrumental broadening and physical broadening of the samples have been measured as full width at half maximum (FWHM). Using corrected physical broadening, we can calculate the average size with the help of Scherrer equation [48-50]. The equation can be explained as follows:

$$D = \frac{b\lambda}{\beta_d} . \frac{1}{cos\theta} \qquad 3.3$$

Where,

$D$ = Average particle size

$\beta_d$ = Angle broadening at the full width half maximum (FWHM),

$\lambda$ = Wavelength of incident x-ray radiation,

$b$ = a constant between 0.89 and 0.94 depending on the function used to fit the peak.

Rearranging equation 3.2, we can write,

$$cos\theta = \frac{0.9\lambda}{D} . \frac{1}{\beta_d} \qquad 3.4$$

Now, plotting a graph of $\frac{1}{\beta_d}$ vs $cos\theta$ for n-Si, p-Si nanoparticles known as the Scherrer plot can provide average particle size from the slope of the graph.

## 3.2 WILLIAMSON-HALL PLOT

The effect of crystallite size on the XRD peak broadening is considered by Scherrer formula, but it does not reveal anything about the micro-structures of the lattice i.e. the intrinsic strain, which is developed in the nanocrystals due to the grain boundary, point defect, triple junction and stacking faults [51, 52]. There are many methods such as Williamsons Hall method, Warren-Averbach method etc., which considers the effect of the strain induced XRD peak broadening and can be used for the calculation of the intrinsic strain along with the particle size. Among these methods, Williamson–Hall (W–H) method is straightforward and simplified one [53, 54]. According to which, physical line broadening of X-ray diffraction peak occurs due to the size and micro-strain of the nanocrystals and the total broadening can be written as,

$$\beta_{total} = \beta_{size} + \beta_{strain} \qquad 3.5$$

### 3.2.1 Uniform deformation model (UDM)

Uniform deformation model (UDM) considers uniform strain throughout the crystallographic direction, which gets introduced in the nanocrystals due to crystal imperfections. In other words, UDM con-siders strain, which is isotropic in nature [55]. This intrinsic strain effects the physical broadening of the XRD profile, and this the strain induced peak broadening can be expressed as.

$$\beta_{strain} = 4\varepsilon . tan\theta \qquad 3.6$$

Size broadening varies as $\frac{1}{cos\theta}$ and the strain broadening varies as $tan\theta$. If both contributions are present, then their combined effect is determined by convolution. The simplification of Williamson-Hall is to assume the convolution is either a simple sum or sum of squares. Using the former of these then we get total broadening having the hkl value,

$$\beta_{hkl} = \beta_{strain} + \beta_{size} = 4\varepsilon . tan\theta + \frac{K\lambda}{D} . \frac{1}{cos\theta} \qquad 3.7$$

After some operations, we get,

$$\beta_{hkl} . cos\theta = \varepsilon(4\, sin\theta) + \frac{K\lambda}{D} \qquad 3.8$$

Equation 3.7 represents a straight line, in which $\varepsilon$ is the gradient (slope) of the line and $\frac{K\lambda}{D}$ is the y-intercept.

Considering the standard equation of a straight line (equation 3.8) we get (equation 3.9 – 3.12),

$$y = mx + c \qquad 3.9$$

$$y = \beta_{hkl} . cos\theta \qquad 3.10$$

$$m = \varepsilon \qquad 3.11$$

$$x = 4 \sin\theta \qquad 3.12$$

$$c = \frac{K\lambda}{D} \qquad 3.13$$

Now if we plot ($4 \sin\theta$) along X-axis and ($\beta_{hkl} . cos\theta$) along Y-axis the value of m which represent gradient (slope) of the line, will indicate the value of the strain $\varepsilon$. And the crystallites size can be calculated from the Y-intercept $\frac{K\lambda}{D}$. The performance of the fitted line can be analyzed from the correlation coefficient value of $R^2$.

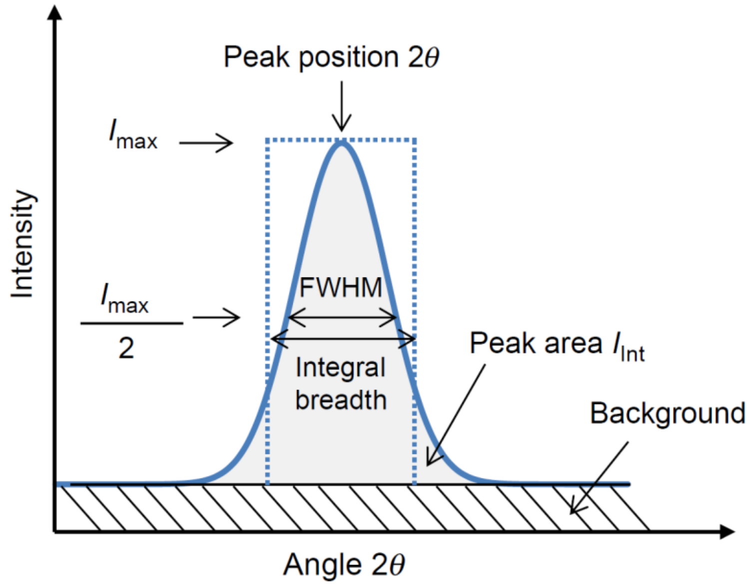


Figure 25: Extracted information content from diffraction peak.

Extracted data from XRD for W-H plot,

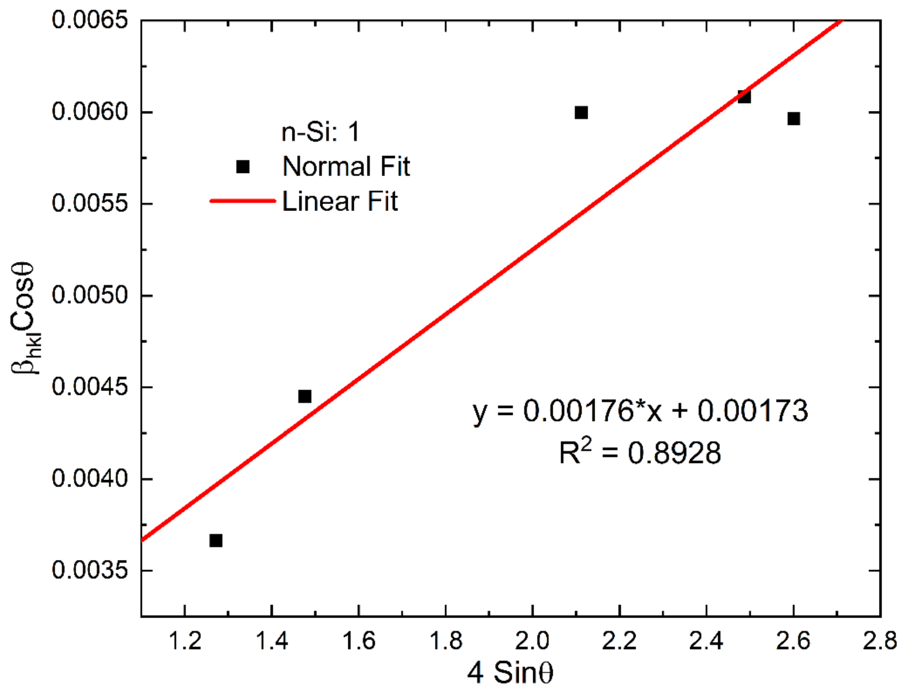


Figure 26(a): UDM plot of RF sputtered n-Si (Sample 1)

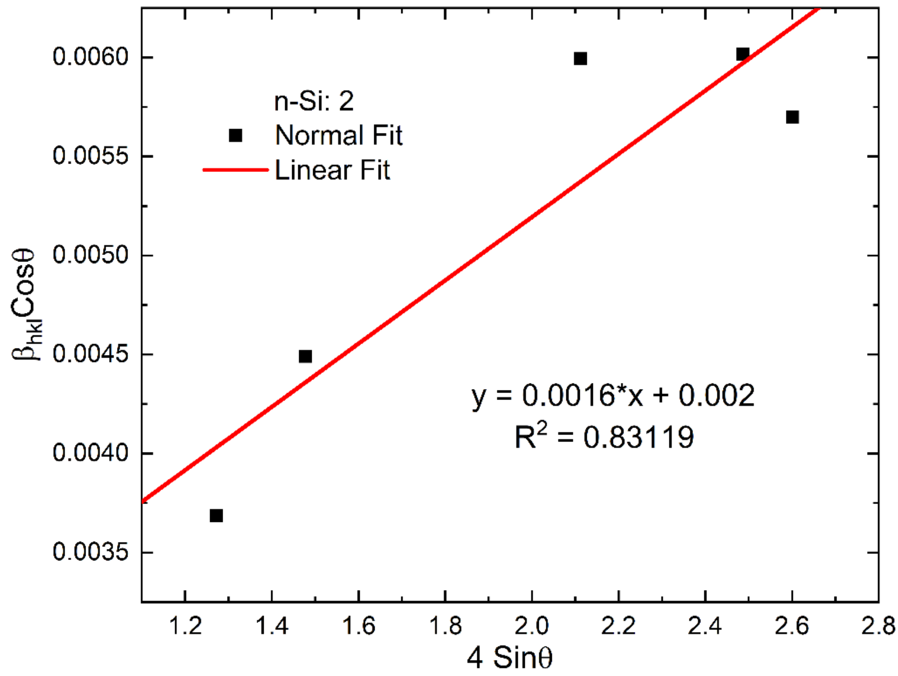


Figure 26(b): UDM plot of RF sputtered n-Si (Sample 2)

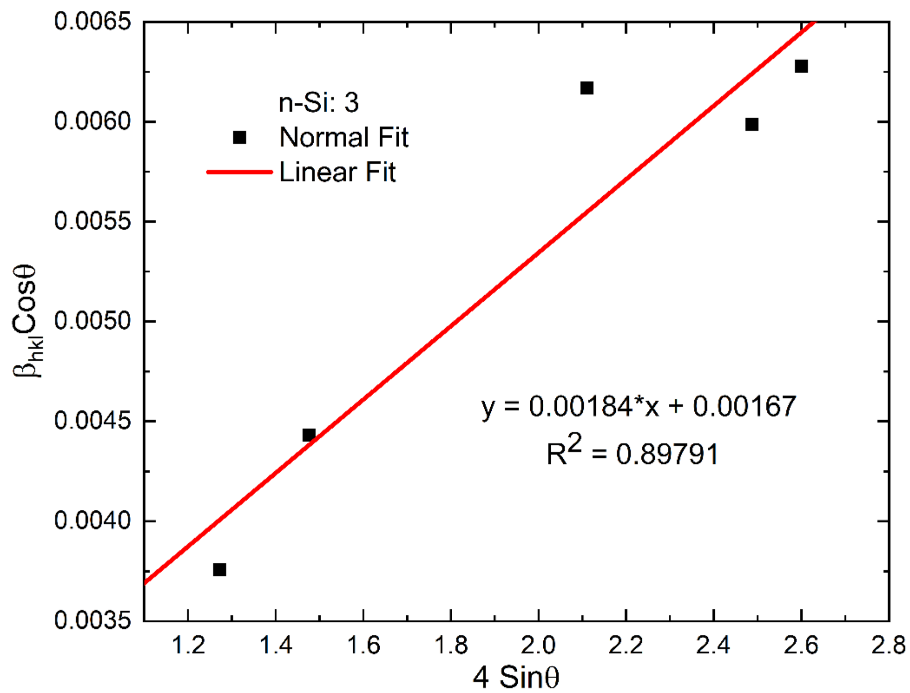


Figure 26(c): UDM plot of RF sputtered n-Si (Sample 3)

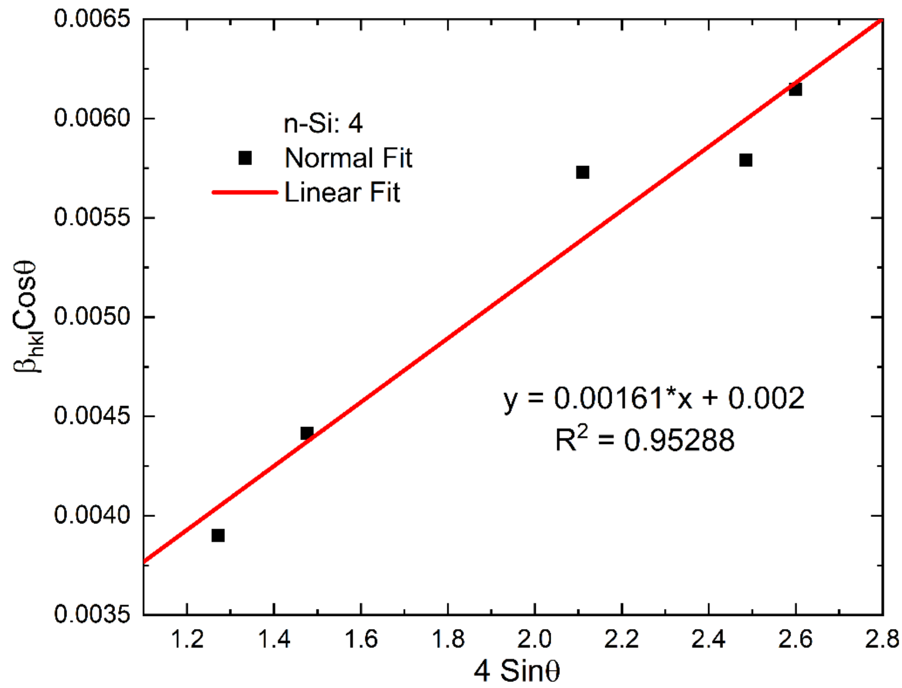


Figure 26(d): UDM plot of RF sputtered n-Si (Sample 4)

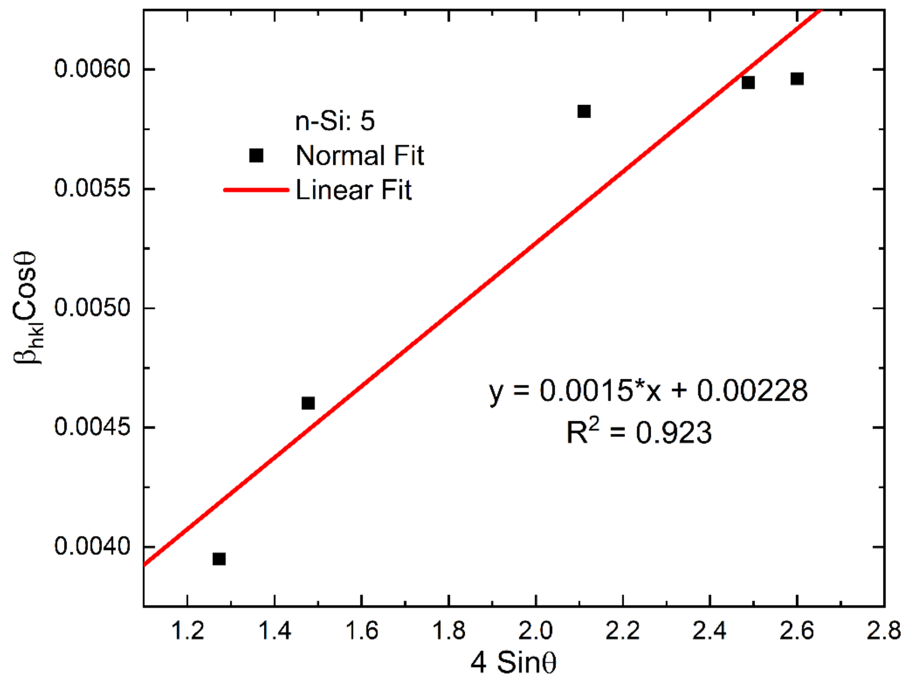


Figure 26(e): UDM plot of RF sputtered n-Si (Sample 5)

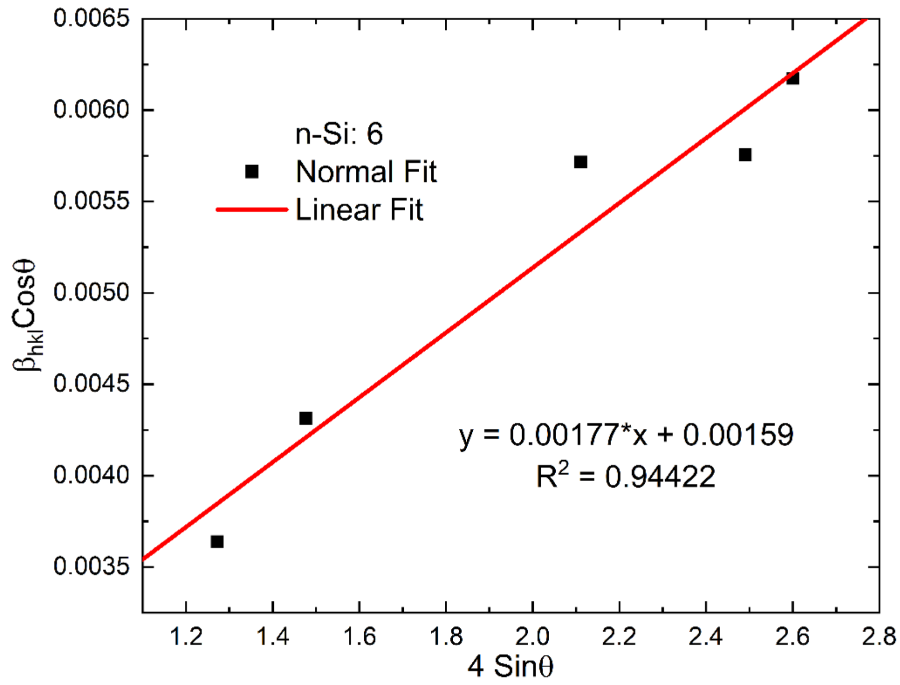


Figure 26(f): UDM plot of RF sputtered n-Si (Sample 6)

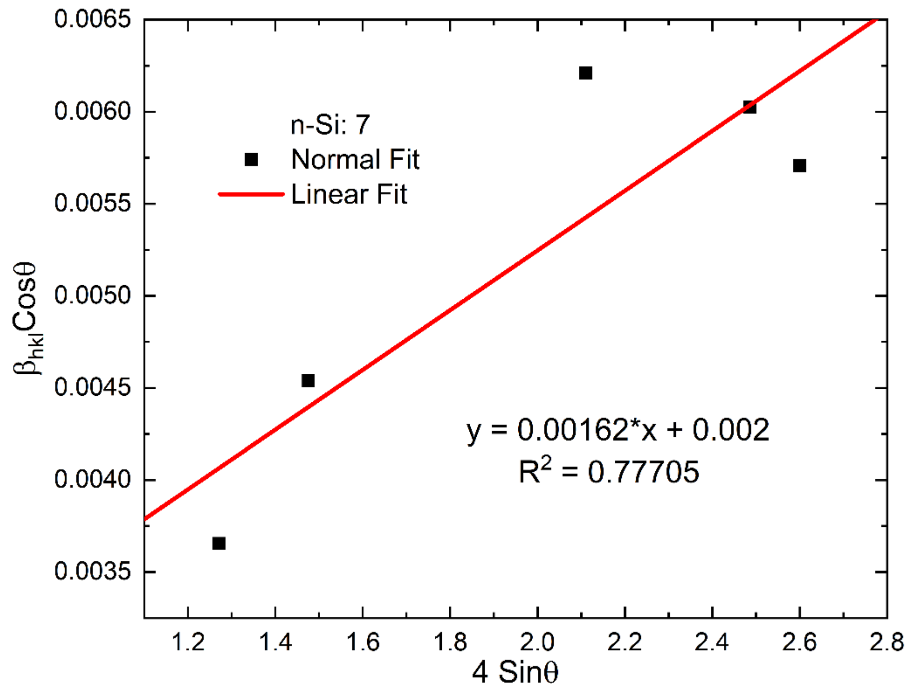


Figure 26(g): UDM plot of RF sputtered n-Si (Sample 7)

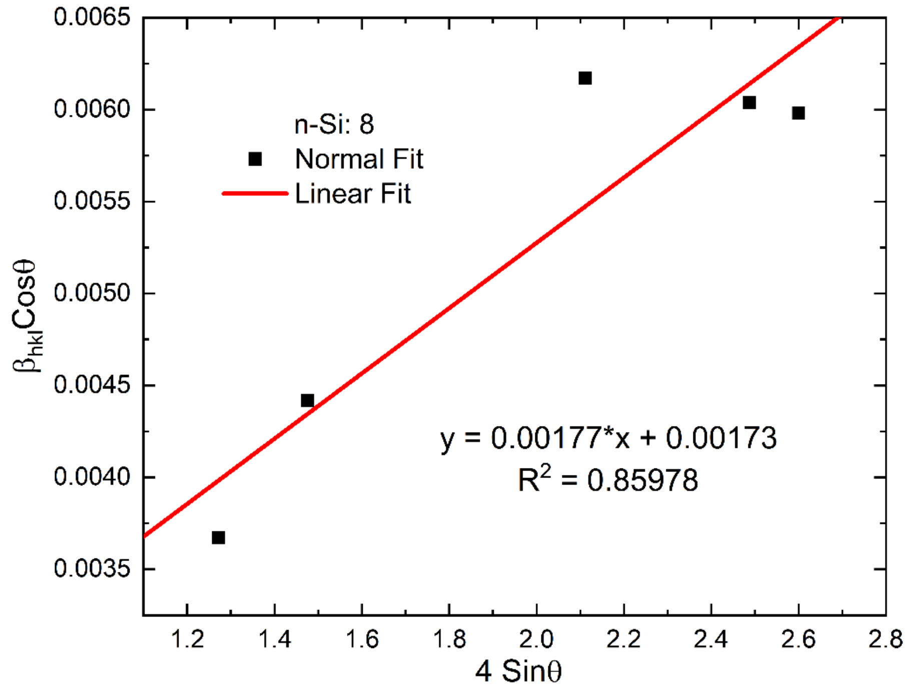


Figure 26(h): UDM plot of RF sputtered n-Si (Sample 8)

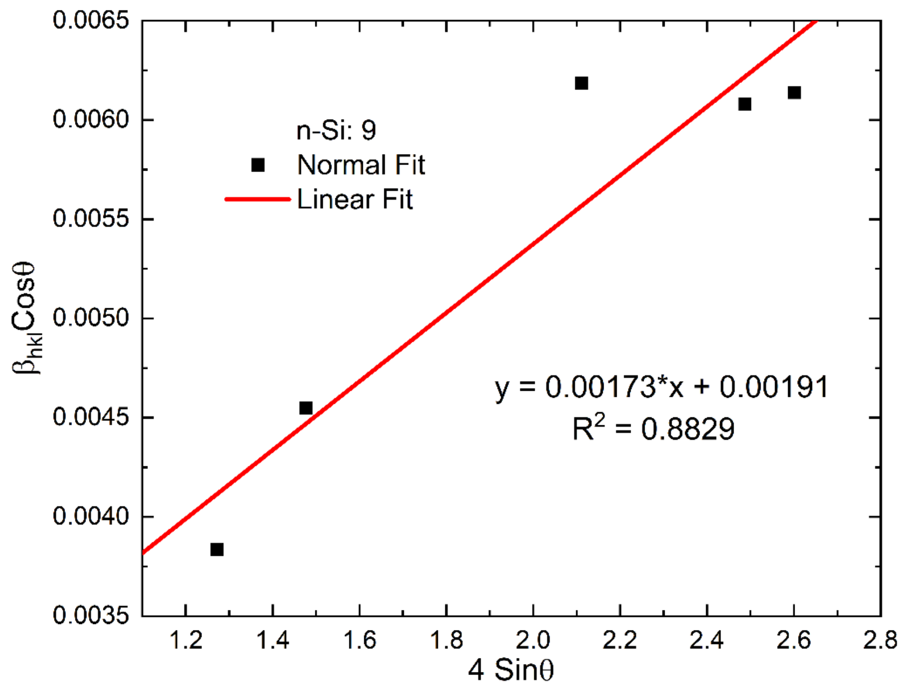


Figure 26(i): UDM plot of RF sputtered n-Si (Sample 9)

# CHAPTER IV

# RESULTS AND DISSCUSSION

## 4.1 SURFACE ROUGHNESS OF n-Si

Roughness is the result of micro-voids and porous on the sputtered thin-film surface. The roughness of the sputtered nSi/Si thin film decreases with increasing RF power indicated by the S/N graph (Figure 6). This result agrees with the theory. When the power is high, the process gas bombard against the target with higher energy, which excited the falling target atom with high energy, therefore forming a densely packed structure filling up most the micro-voids and porous in the surface. Working pressure on the other hand has opposite effect. High pressure means less mean free path between Ar gas atoms, so the falling target atom faces more inter-atomic collision, restraining the kinetic energy of the target atom. Loosely packed structure with high porosity forms up over the substrate. Our experimental data, as shown in Figure 6 also matches with this theory, as well as with the previous works[56, 57]. At low working pressure and high RF power, very high energetic bombardment near the surface, which is called “peening effect” [56-59] produces a very smooth surface.

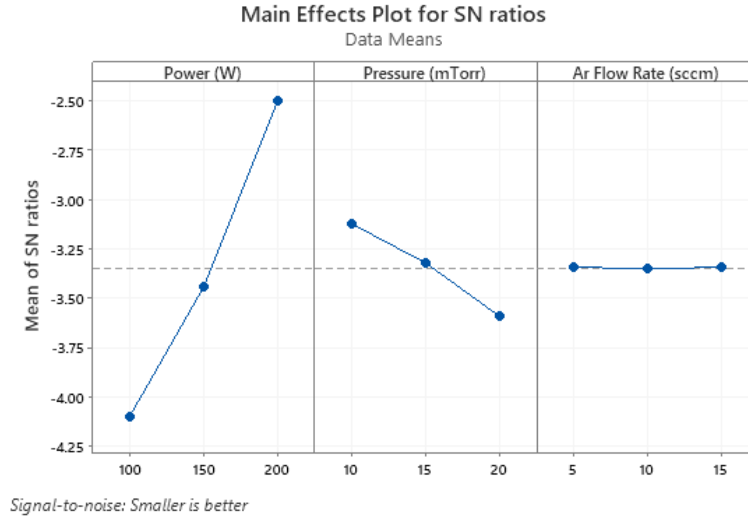


Figure 27: S/N response graph for the surface roughness of the nSi/Si films.

Table 4: Analysis of variance for surface roughness

| Source | DOF | Seq. SS | Contribution | F Value | P value |
|---|---|---|---|---|---|
| Power | 2 | 0.110022 | 91.82% | 1237.75 | 0.001 |
| Pressure | 2 | 0.009689 | 8.09% | 109.00 | 0.009 |
| Ar flow rate | 2 | 0.000022 | 0.02% | 0.25 | 0.800 |
| Error | 2 | 0.000089 | 0.07% | | |
| Total | 8 | 0.119822 | 100.00% | | |

From the ANOVA analysis, we found that the contribution of power is dominant (91.82%) to the surface roughness. Working Pressure has lesser contribution (8.09%) whereas Ar gas flow rate has no significant effect at all. Using our experimental data, a regression model was derived in case a thin film with a particular roughness is desired which is given below,

$$Roughness(nm) = 1.7156 - 0.00270\ Power\ (W) + 0.00800\ Pressure\ (mT) + 0.00033\ Ar\ rate\ (sccm)$$

Table 5: Model summary of the regression equation

| S | R-sq | R-sq (adj) | R-sq (pred) |
|---|---|---|---|
| 0.0130809 | 99.29% | 98.86% | 97.89% |

Table 6: Summery of n-Si/Si thin films characterizations

| Sample no. | Roughness (nm) | Williamson-Hall Method | | | |
|---|---|---|---|---|---|
| | | Grain Size D (nm) | Strain ($\varepsilon$) ($* 10^{-3}$) | Dislocation density ($cm^{-2}$) ($* 10^{10}$) | Determination Coeff. ($R^2$) |
| Sample 1 | 1.56 | 80.14682 | 1.76 | 1.5568 | 90.8928 |
| Sample 2 | 1.60 | 69.32700 | 1.60 | 2.0806 | 0.83119 |
| Sample 3 | 1.65 | 83.02635 | 1.84 | 1.4507 | 0.89791 |
| Sample 4 | 1.45 | 88.03430 | 1.61 | 1.2903 | 0.95288 |
| Sample 5 | 1.48 | 60.81316 | 1.50 | 2.7040 | 0.92300 |
| Sample 6 | 1.53 | 87.20377 | 1.77 | 1.3150 | 0.94422 |
| Sample 7 | 1.30 | 65.93000 | 1.62 | 2.3005 | 0.77705 |
| Sample 8 | 1.33 | 80.14682 | 1.77 | 1.5568 | 0.85978 |
| Sample 9 | 1.37 | 72.59372 | 1.73 | 1.8976 | 0.88290 |

## 4.2 CRYSTAL FORMATION OF n-Si

The high crystallinity was evident from the sharp and intense peaks of RF sputtered n-Si thin films (figure 4). The crystallite size of the films were found to vary from 65.93 nm to 88.0343

nm. From experimental data it was found that the grain size increased with power at first and then started to decrease at higher levels. This was attributed to sufficient kinetic energy of plasma ions which directly depends upon sputtering power. Kinetic energy of incident plasma ions increased with the increase of sputtering power resulted in the rise of nucleation sites and growth rate. If the growth rate in lateral direction is better than nucleation rate, size of the grain increases. Further increase in power improves nucleation density and prevents lateral growth of crystallites that results in the reduction of crystallite size. The theory matched with the S/N response of figure 7. Higher grain size was obtained at lower Ar flow rate and at high Ar pressure.

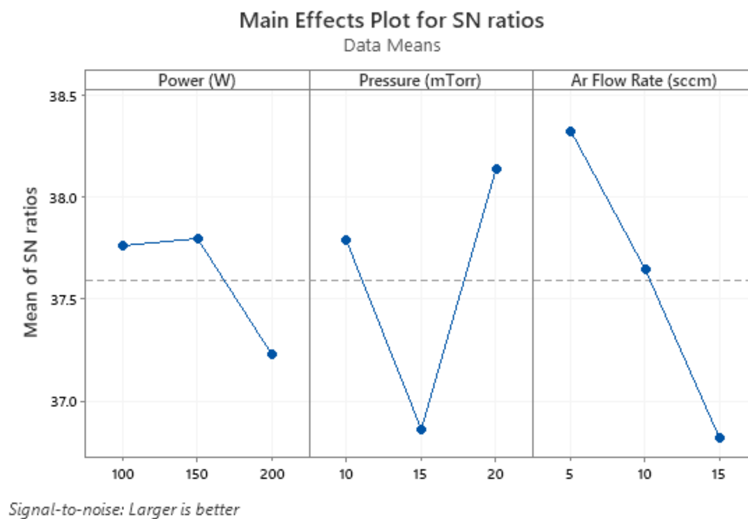


Figure 28: S/N response graph for the grain size of the n-Si thin films.

Table 7 Analysis of variance for grain size

| Source | DOF | Seq. SS | Contribution | F Value | P value |
|---|---|---|---|---|---|
| Power | 2 | 56.22 | 7.59% | 0.22 | 0.821 |
| Pressure | 2 | 189.13 | 25.52% | 0.73 | 0.577 |

| | | | | | |
|---|---|---|---|---|---|
| Ar flow | 2 | 237.62 | 32.06% | 0.92 | 0.521 |
| Error | 2 | 258.17 | 34.83% | | |
| Total | 8 | 741.13 | 100.00% | | |

From ANOVA analysis (table 7) no individual contribution of the process parameters was found. Among all three factors, contribution of pressure (25.52%) and Ar flow rate (32.06%) was more compared to the RF power contribution (7.59%).

### 4.3 MICRO-STRAIN OF n-Si

Good adhesion to the Si substrate and low residual stress within the films are essential attributes to ensure reliability of n-Si thin films. The micro strain of all the sputtered n-Si thin films was determined from the gradient of the fitted lines of W-H plot. All films were found to be under a state of compressive stress, as the films were sputtered using a cylindrical rotating magnetron which tends to yield high plasma density. Another reason for the compressive stress state could be that the working distance for deposition, which is lower than the mean free path of the sputtered ions. The increase in stress was attributed to the saturated nucleation density resulted into higher growth rates in lateral direction. Form S/N graph (Figure 8) highest amount of strain was observed at 150 W, 15 mT and 10 sccm Ar flow rate. The highest micro strain was attributed to the same nucleation density and growth rate at 150 W of sputtering power. Beyond 150 W power, the stress was relieved as higher growth rate and increase in subsequent number of nucleation sites. Similar stress profile was observed with the Ar pressure and Ar flow rate. First increased with Ar flow rate up to 10 sccm and decreased after that as shown in S/N graph. This can be attributed to atomic peeing effect of incident carrier ions having lower kinetic energy with increase in Ar gas flow rate, as discussed by D’Heurle et al.[60]. The increase in compressive

stress at 10 sccm Ar gas flow was a result of the dense highly ordered nature of the films at saturated kinetic energy of incident plasma ions and saturated nucleation density.

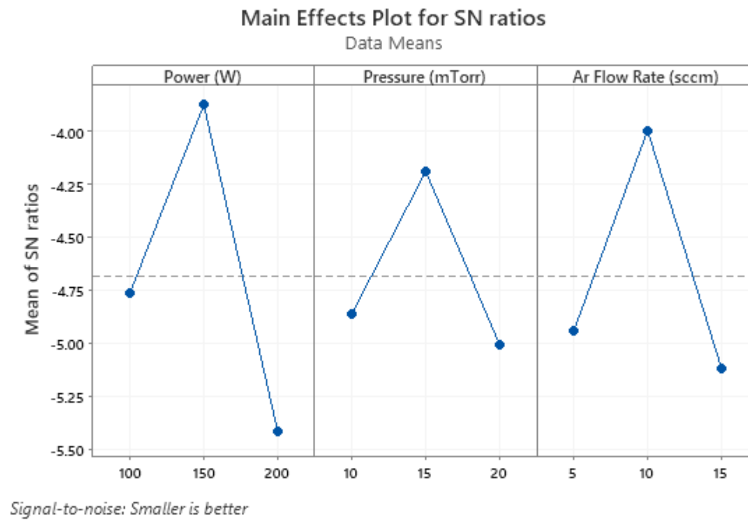


Figure 29: S/N response graph for the micro strain of the n-Si thin films

The ANOVA test (table 8) indicated power to be the most effective parameter among all others. It contributed 43.02% while Ar flow 27.17% and pressure 14.34%.

Table 8: Analysis of variance for micro-strain

| Source | DOF | Seq. SS | Contribution | F Value | P value |
|---|---|---|---|---|---|
| Power | 2 | 0.14044 | 43.02% | 2.78 | 0.265 |
| Pressure | 2 | 0.04680 | 14.34% | 0.93 | 0.519 |
| Ar flow | 2 | 0.08870 | 27.17% | 1.76 | 0.363 |
| Error | 2 | 0.05054 | 15.48% | | |
| Total | 8 | 0.32648 | 100.00% | | |

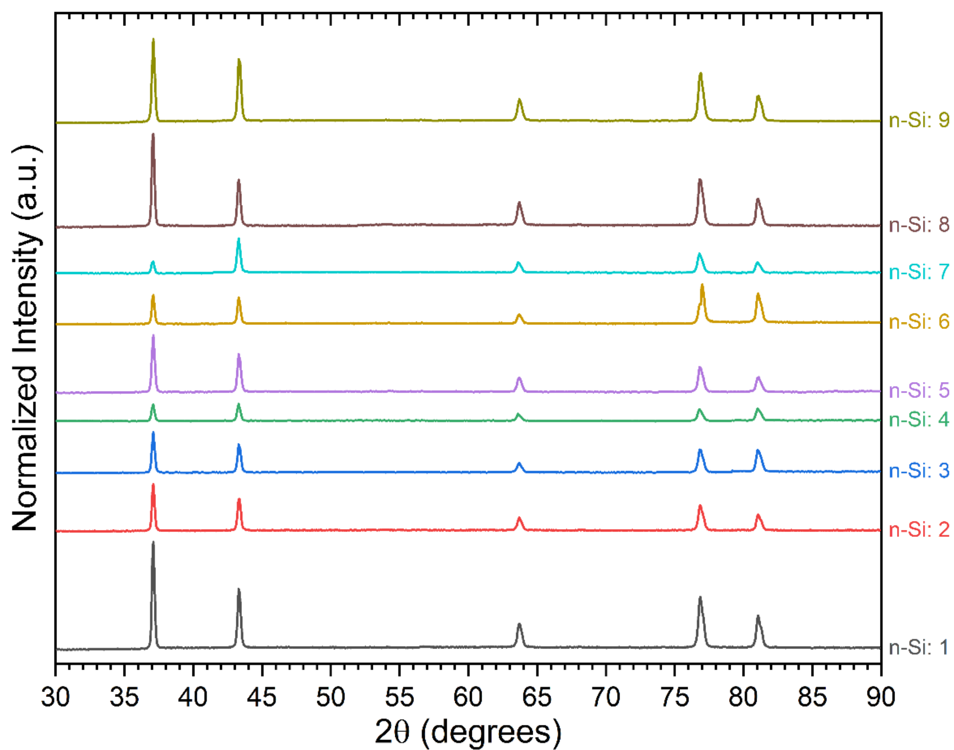


Figure 30: XRD pattern of RF sputtered n-Si in normalized intensity (9 samples )

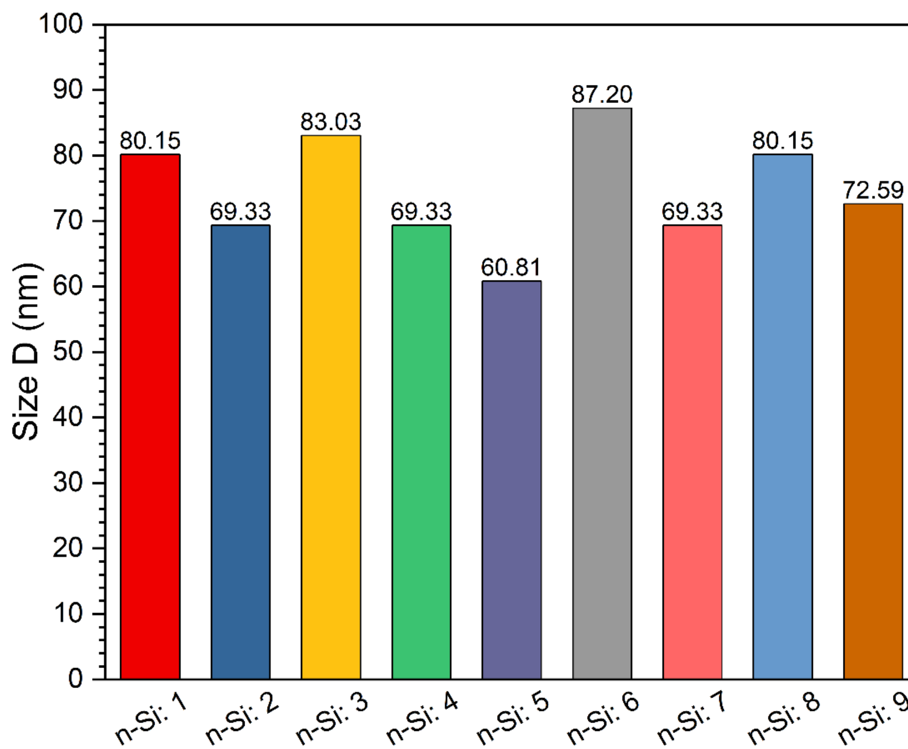


Figure 31: Grain size of all n-Si samples

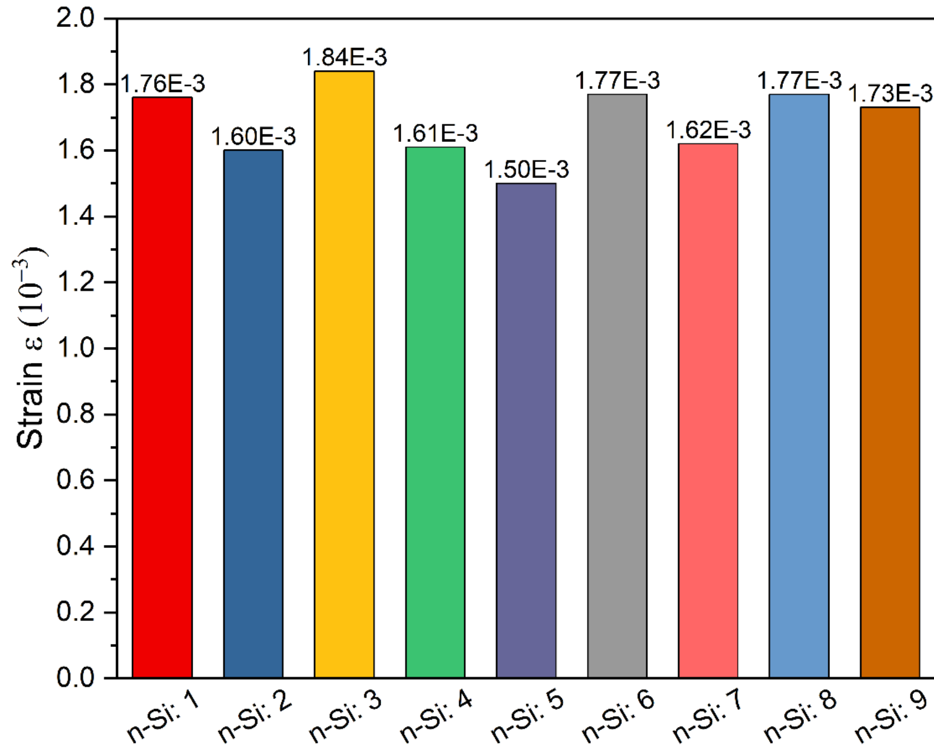


Figure 32: Micro strain of all n-Si samples

## 4.4 SURFACE ROUGHNESS OF p-Si

Table 9: Overall measured outputs for p-Si samples

| **Sample Number of p-Si** | Input Parameters | | | Base Pressure | Outputs | |
|---|---|---|---|---|---|---|
| | Power (Watt) | Pressure (mTorr) | Ar Flow (sccm) | Torr | Roughness (nm) | Grain size (nm) |
| Sample 1 | 100 | 10 | 5 | 4.88E-6 | 2.20 | 88.66 |
| Sample 2 | 100 | 15 | 10 | 2.37E-6 | 2.27 | 82.13 |
| Sample 3 | 100 | 20 | 15 | 4.95E-6 | 2.37 | 77.74 |
| Sample 4 | 150 | 10 | 10 | 1.73E-6 | 1.97 | 112.12 |
| Sample 5 | 150 | 15 | 15 | 1.50E-6 | 1.85 | 112.23 |
| Sample 6 | 150 | 20 | 5 | 2.98E-6 | 2.46 | 65.05 |

| Sample 7 | 200 | 10 | 15 | 1.30E-6 | 1.47 | 85.97 |
|---|---|---|---|---|---|---|
| Sample 8 | 200 | 15 | 5 | 1.34E-6 | 1.68 | 71.54 |
| Sample 9 | 200 | 20 | 10 | 1.10E-6 | 1.80 | 57.61 |

Table 10: ANOVA analysis for surface roughness of p-Si

| **Source of variation** | **DF** | **Seq SS** | **Contribution** | **Adj SS** | **Adj MS** | **F-Value** | **P-value** |
|---|---|---|---|---|---|---|---|
| Power (Watt) | 2 | 0.62829 | 69.23% | 0.62829 | 0.31414 | 30.76 | 0.031 |
| Pressure (mTorr) | 2 | 0.18829 | 20.75% | 0.18829 | 0.09414 | 9.22 | 0.098 |
| Ar Flow (sccm) | 2 | 0.07056 | 7.77% | 0.07056 | 0.03528 | 3.45 | 0.224 |
| Error | 2 | 0.02042 | 2.25% | 0.02042 | 0.01021 | | |
| Total | 8 | 0.90756 | 100% | | | | |

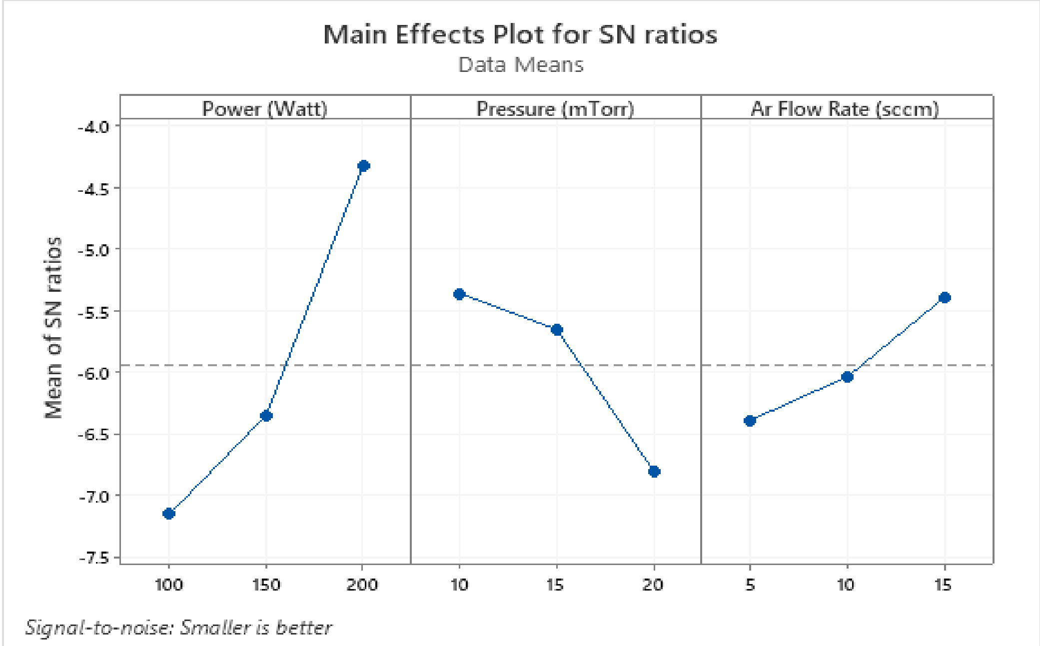


Figure 33: S/N response graph for the roughness of the pSi films with RF power (Watt), Pressure (mTorr) and Ar Flow (sccm).

**Regression Equation:**

Roughness (nm) = 2.674 ─ 0.00630 Power (W) + 0.0330 Pressure (mTorr) ─ 0.0217 Ar Flow (sccm)

**Model Summary:**

| S | R-Sq | R-Sq (adj) | R-Sq (pred) |
|---|---|---|---|
| 0.125251 | 91.36% | 86.17% | 72.51% |

## 4.5 CRYSTAL FORMATION OF p-Si

Table 11: ANOVA analysis for p-Si grain size

| **Source of variation** | **DF** | **Seq SS** | **Contribution** | **Adj SS** | **Adj MS** | **F-Value** | **P-value** |
|---|---|---|---|---|---|---|---|
| Power (Watt) | 2 | 920.1 | 32.17% | 920.1 | 460.05 | 5.74 | 0.148 |
| Pressure (mTorr) | 2 | 1350.6 | 47.23% | 1350.6 | 675.31 | 8.43 | 0.106 |
| Ar Flow (sccm) | 2 | 428.9 | 15.00% | 428.9 | 214.44 | 2.68 | 0.272 |
| Error | 2 | 160.2 | 5.60% | 160.2 | 80.08 | | |
| Total | 8 | 2859.8 | 100.00% | | | | |

**Regression Equation:**

Grain Size (nm) = 126.6 - 0.111 Power (Watt) - 2.87 Pressure (mTorr) + 1.69 Ar Flow Rate (sccm)

**Model Summary:**

| S | R-Sq | R-Sq (adj) | R-Sq (pred) |
|---|---|---|---|
| 14.1828 | 64.83% | 43.73% | 0.00% |

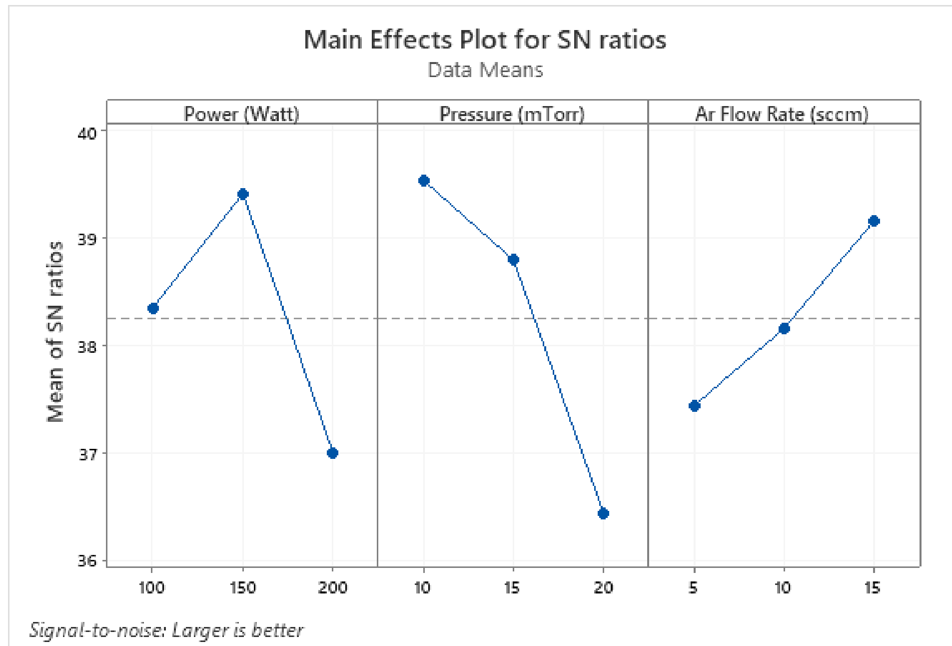


Figure 34: S/N response graph for the Grain size of the pSi films with RF power (Watt), Pressure (mTorr) and Ar Flow (sccm).

# CHAPTER V

## CONCLUSSION AND FUTURE WORK

Nine samples of n-Si/Si thin films were sputtered at 3 power levels, 3 Ar flow rates and 3 Ar gas pressure levels to optimize the process for achieving the desired surface and morphological properties. The surface roughness observed to be lowest at low RF power and high Ar pressure, while largest grain size is observed mostly at low Ar flow rate and at mid-level RF processing power of 150 W. Highest strain was observed at 150 W, 15 mT and 10 sccm Ar flow rate.

REFERENCES

1. El-Kareh, B. and L.N. Hutter, *Fundamentals of semiconductor processing technology*. 2012: Springer Science & Business Media.

2. Judy, J.W., *Microelectromechanical systems (MEMS): fabrication, design and applications.* Smart materials and Structures, 2001. 10(6): p. 1115.

3. Tilli, M., et al., *Handbook of silicon based MEMS materials and technologies*. 2020: Elsevier.

4. Sato, K., et al., *The synthesis and structural characterization of boron-doped silicon-nanocrystals with enhanced electroconductivity.* Nanotechnology, 2009. 20(36): p. 365207.

5. Chopra, S., et al., *Heavily phosphorus doped silicon junctions for nMOS applications.* ECS Transactions, 2008. 13(1): p. 307.

6. Weeks, K., et al., *Characterization and analysis of epitaxial silicon phosphorus alloys for use in n-channel transistors.* Thin Solid Films, 2012. 520(8): p. 3158-3162.

7. Zaidan, K., et al., *Synthesis and characterization of (Pani/n-si) solar cell.* Energy procedia, 2011. 6: p. 85-91.

8. Lee, J., et al., *Defect generation mechanism of epitaxially grown in situ phosphorus-doped silicon on silicon (111) substrate.* physica status solidi (a), 2020. 217(12): p. 1900990.

9. Bauer, M. and S. Thomas, *Low temperature Si: C co-flow and hybrid process using Si3H8/Cl2.* Thin Solid Films, 2012. 520(8): p. 3133-3138.

10. Lee, M., E. Ko, and D.-H. Ko, *Probing lattice vibration and strain states in highly phosphorus-doped epitaxial Si films.* Journal of Materials Chemistry C, 2017. 5(37): p. 9744-9752.

11. Rosseel, E., et al., *Selective epitaxial growth of high-P Si: P for source/drain formation in advanced Si nFETs.* ECS Transactions, 2016. 75(8): p. 347.

12. Yeo, Y.-C., *Enhancing CMOS transistor performance using lattice-mismatched materials in source/drain regions.* Semiconductor science and technology, 2006. 22(1): p. S177.

13. Bedell, S., A. Khakifirooz, and D. Sadana, *Strain scaling for CMOS.* Mrs Bulletin, 2014. 39(2): p. 131-137.

14. Chu, M., et al., *Strain: A solution for higher carrier mobility in nanoscale MOSFETs.* Annual Review of Materials Research, 2009. 39: p. 203-229.

15. Wang, G., et al. *Preparation methods and application of silicon oxide films*. in *2014 International Conference on Mechatronics, Electronic, Industrial and Control Engineering (MEIC-14)*. 2014. Atlantis Press.

16. Hoex, B., et al., *High-rate plasma-deposited Si O 2 films for surface passivation of crystalline silicon.* Journal of Vacuum Science & Technology A: Vacuum, Surfaces, and Films, 2006. 24(5): p. 1823-1830.

17. Li, W., et al., *The effect of defects on the optical nonlinearity of thermally poled SiOx thin films.* Thin Solid Films, 2008. 516(16): p. 5474-5477.

18. Creatore, M., F. Palumbo, and R. d'Agostino, *Diagnostics and insights on PECVD for gas-barrier coatings.* Pure and applied chemistry, 2002. 74(3): p. 407-411.

19. Vautrin-Ul, C., et al., *Hexamethyldisiloxane (HMDSO)-plasma-polymerised coatings as primer for iron corrosion protection: influence of RF bias.* Journal of Materials Chemistry, 2002. 12(8): p. 2318-2324.
20. Delimi, A., et al., *Investigation of the corrosion protection of SiOx-like oxide films deposited by plasma-enhanced chemical vapor deposition onto carbon steel.* Electrochimica acta, 2010. 55(28): p. 8921-8927.
21. Hsu, H.-L., et al., *Electrical and optical studies of Ga-doped ZnO thin films.* Journal of Materials Science: Materials in Electronics, 2013. 24(1): p. 13-19.
22. Huang, P.-c., et al., *The effect of sputtering parameters on the film properties of molybdenum back contact for CIGS solar cells.* International Journal of Photoenergy, 2013. 2013.
23. Patel, S.B. and J.V. Gohel, *Enhanced solar cell performance by optimization of spray coated CZTS thin film using Taguchi and response surface method.* Journal of Materials Science: Materials in Electronics, 2018. 29(7): p. 5613-5623.
24. Vashaei, Z., et al., *Influence of sputtering parameters on the crystallinity and crystal orientation of AlN layers deposited by RF sputtering using the AlN target.* Journal of Crystal Growth, 2009. 311(3): p. 459-462.
25. Boulmani, R., et al., *Correlation between rf-sputtering parameters and WO3 sensor response towards ozone.* Sensors and Actuators B: Chemical, 2007. 125(2): p. 622-627.
26. Bhatt, V. and S. Chandra, *Silicon dioxide films by RF sputtering for microelectronic and MEMS applications.* Journal of micromechanics and microengineering, 2007. 17(5): p. 1066.

27. Jindrich Musil, J.V., Pavel Baroch, *Chapter 3 - Magnetron Discharges for Thin Films Plasma Processing*. Elsevier, 2006: p. 67-110.

28. *Principles of Plasma Discharges and Materials Processing*, in *Principles of Plasma Discharges and Materials Processing*. 2005. p. 1-22.

29. Musil, J., et al., *Structure and properties of magnetron sputtered Zr–Si–N films with a high (≥ 25 at.%) Si content.* Thin Solid Films, 2005. 478(1-2): p. 238-247.

30. Vlček, J., et al., *Benefits of the controlled reactive high-power impulse magnetron sputtering of stoichiometric ZrO2 films.* Vacuum, 2015. 114: p. 131-141.

31. Zou, Y., H. Ma, and R. Spolenak, *Ultrastrong ductile and stable high-entropy alloys at small scales.* Nature communications, 2015. 6(1): p. 1-8.

32. Pearce, S., et al., *Structural characteristics and optical properties of plasma assisted reactive magnetron sputtered dielectric thin films for planar waveguiding applications.* Surface and Coatings Technology, 2012. 206(23): p. 4930-4939.

33. Mayrhofer, P., C. Mitterer, and J. Musil, *Structure–property relationships in single-and dual-phase nanocrystalline hard coatings.* Surface and Coatings Technology, 2003. 174: p. 725-731.

34. Mayrhofer, P.H., et al., *Microstructural design of hard coatings.* Progress in materials science, 2006. 51(8): p. 1032-1114.

35. Musil, J., et al., *ZrN/Cu nanocomposite film—a novel superhard material.* Surface and Coatings Technology, 1999. 120: p. 179-183.

36. Petrov, I., et al., *Microstructure modification of TiN by ion bombardment during reactive sputter deposition.* Thin Solid Films, 1989. 169(2): p. 299-314.

37. Furrer, A. and R. Spolenak, *Colors of thin films of binary and ternary gold-and platinum-based alloys.* Acta materialia, 2014. 66: p. 241-250.

38. Zenkin, S., *Reaktivní magnetronové naprašování tenkých vrstev s unikálními vlastnostmi.* 2017.

39. Compaan, A.D., et al., *High efficiency, magnetron sputtered CdS/CdTe solar cells.* Solar Energy, 2004. 77(6): p. 815-822.

40. Charpentier, C., *Investigation of deposition conditions and annealing treatments on sputtered ZnO:Al thin films: Material properties and application to microcristalline silicon solar cells*. 2012, Ecole Polytechnique X.

41. Musil, J., et al., *Reactive magnetron sputtering of thin films: present status and trends.* Thin solid films, 2005. 475(1-2): p. 208-218.

42. Salehuddin, F., et al. *Optimization of process parameter variation in 45nm p-channel MOSFET using L 18 orthogonal array*. in *2012 10th IEEE International Conference on Semiconductor Electronics (ICSE)*. 2012. IEEE.

43. Kim, S.J., K.S. Kim, and H. Jang, *Optimization of manufacturing parameters for a brake lining using Taguchi method.* Journal of Materials Processing Technology, 2003. 136(1-3): p. 202-208.

44. Delhez, R., T.H. De Keijser, and E. Mittemeijer, *Determination of crystallite size and lattice distortions through X-ray diffraction line profile analysis.* Fresenius' Zeitschrift für analytische Chemie, 1982. 312(1): p. 1-16.

45. Das, R., S.S. Nath, and R. Bhattacharjee, *Preparation of linoleic acid capped gold nanoparticles and their spectra.* Physica E: Low-dimensional Systems and Nanostructures, 2010. 43(1): p. 224-227.

46. Dey, P. and R. Das, *Effect of silver doping on the elastic properties of CdS nanoparticles.* Indian Journal of Physics, 2018. 92(9): p. 1099-1108.

47. Yogamalar, R., et al., *X-ray peak broadening analysis in ZnO nanoparticles.* Solid State Communications, 2009. 149(43-44): p. 1919-1923.

48. Bindu, P. and S. Thomas, *Estimation of lattice strain in ZnO nanoparticles: X-ray peak profile analysis.* Journal of Theoretical and Applied Physics, 2014. 8(4): p. 123-134.

49. Zak, A.K., et al., *X-ray analysis of ZnO nanoparticles by Williamson–Hall and size–strain plot methods.* Solid State Sciences, 2011. 13(1): p. 251-256.

50. De, M. and S.S. Gupta, *Lattice imperfection studies in polycrystalline materials by x-ray diffraction line-profile analysis.* Pramana, 1984. 23(6): p. 721-744.

51. Das, R. and S. Sarkar, *Determination of intrinsic strain in poly (vinylpyrrolidone)-capped silver nano-hexapod using X-ray diffraction technique.* Current Science, 2015: p. 775-778.

52. Balzar, D. and H. Ledbetter, *Voigt-function modeling in Fourier analysis of size-and strain-broadened X-ray diffraction peaks.* Journal of Applied Crystallography, 1993. 26(1): p. 97-103.

53. Warren, B. and B. Averbach, *The separation of cold-work distortion and particle size broadening in X-ray patterns.* Journal of applied physics, 1952. 23(4): p. 497-497.

54. Jacob, R. and J. Isac, *X-ray diffraction line profile analysis of Ba0. 6Sr0. 4FexTi (1− x) O3-δ,(x= 0.4).* Int. J. Chem. Stud, 2015. 2: p. 12-21.

55. Birks, L. and H. Friedman, *Particle size determination from X-ray line broadening.* Journal of Applied Physics, 1946. 17(8): p. 687-692.

56. Huff, M.A., A.D. Nikolich, and M.A. Schmidt. *A threshold pressure switch utilizing plastic deformation of silicon*. in *TRANSDUCERS'91: 1991 International Conference on Solid-State Sensors and Actuators. Digest of Technical Papers*. 1991. IEEE.

57. Hurley, R. and H. Gamble, *Thin film sputtered silicon for silicon wafer bonding applications.* Vacuum, 2003. 70(2-3): p. 131-140.

58. Pal, P. and S. Chandra, *RF sputtered silicon for MEMS.* Journal of Micromechanics and Microengineering, 2005. 15(8): p. 1536.

59. Wu, H.-M., et al., *Structure and electrical properties of Mo back contact for Cu (In, Ga) Se2 solar cells.* Vacuum, 2012. 86(12): p. 1916-1919.

60. d'Heurle, F. and J. Harper, *Note on the origin of intrinsic stresses in films deposited via evaporation and sputtering.* Thin Solid Films, 1989. 171(1): p. 81-92.

# APPENDIX

## APPENDIX A

## GLOSSARY

Band gap : A band gap is the distance between the valence band of electrons and the conduction band.

CMOS : refers to both a particular style of digital circuitry design and the family of processes used to implement that circuitry on integrated circuits (chips)

Crystal structure : In crystallography, crystal structure is a description of the ordered arrangement of atoms, ions or molecules in a crystalline material.

CVD : Chemical vapor deposition (CVD) is a vacuum deposition method used to produce high quality, high-performance, solid materials.

DOE : Design of Experiment

Doping : In semiconductor production, doping is the intentional introduction of impurities into an intrinsic semiconductor for the purpose of modulating its electrical, optical and structural properties.

Electron Beam : Stream of electrons generated by heat (thermionic emission), bombardment of charged atoms or particles (secondary electron emission), or strong electric fields (field emission).

Epitaxial Growth : Epitaxial growth is broadly defined as the condensation of gas precursors to form a film on a substrate. Liquid precursors are also used, although the vapor phase from molecular beams is more in use.

F-value : The F value in regression is the result of a test where the null hypothesis is that all the regression coefficients are equal to zero.

Ion-implantation : Ion implantation is a low-temperature process by which ions of one element are accelerated into a solid target, thereby changing the physical, chemical, or electrical properties of the target.

MEMS: A MEMS (micro-electromechanical system) is a miniature machine that has both mechanical and electronic components.

N-type semiconductor: An extrinsic semiconductor which has been doped with electron donor atoms is called an n-type semiconductor, because most charge carriers in the crystal are negative electrons.

Optoelectronics : Optoelectronics is the study and application of electronic devices that use light. Such devices include those that emit light (LEDs and light bulbs), channel light (fiber optic cables), detect light (photodiodes and photoresistors), or are controlled by light (opto-isolators and phototransistors).

Plasma: Plasma is called the fourth state of matter after solid, liquid, and gas. It is a state of matter in which an ionized substance becomes highly electrically conductive to the point that long-range electric and magnetic fields dominate its behaviour.

P-value : The p value is the evidence against a null hypothesis. The smaller the p-value, the stronger the evidence that you should reject the null hypothesis.

P-type semiconductor : P-type semiconductors are created by doping an intrinsic semiconductor with an electron acceptor element during manufacture.

PVD : Physical Vapor Deposition

Sputtering : In physics, sputtering is a phenomenon in which microscopic particles of a solid material are ejected from its surface, after the material is itself bombarded by energetic particles of a plasma or gas.

S-value : S represents the average distance that the observed values fall from the regression line.

TFT : Thin Film Transistor

BIOGRAPHICAL SKETCH

Prosanto Biswas has received a B.S degree in electrical and electronic engineering from the Bangladesh University of Engineering and Technology, Dhaka, in 2017. He joined the Electrical Engineering Department at the University of Texas Rio Grande Valley in 2019. Since then, he had been working at the Sputtering System Lab under Dr. Hasina F. Huq's supervision. He had also worked as Graduate Teaching Assistant under Dr. Yoonsu (Paul) Choi, Dr. Jaime Ramos Salas, Dr. Wenjie Dong, Dr. Nazmul Islam, Dr. Yong Zhou, Dr. Jungfei Li, Dr. Samir Iqbal, and Dr. Hasina F. Huq. He earned his Master of Science in Engineering degree from the University of Texas Rio Grande Valley in May 2021. His research interest includes thin-film transistors, wide bandgap semiconductors, nanomaterials, nanoengineered Devices, and Bio-MEMS/NEMS. He received the prestigious Presidential Graduate Research Assistantship (2019-2020), He became the Champion at the poster competition of the college of science (COS) annual research conference 2020 and stood 1st runner up at the college of engineering annual E-Week poster competition 2021. So far, he has published 2 conference papers, and 2 more are underway. He is expected to join the University of Texas at Dallas in Fall 2021 for Ph.D. in Electrical and Computer Engineering. He can be reached at prosanto.biswas224@gmail.com.